INFORMATION TO USERS

This manuscript has been reproduced from the microfilm master. UMI films the text directly from the original or copy submitted. Thus, some thesis and dissertation copies are in typewriter face, while others may be from any type of computer printer.

The quality of this reproduction is dependent upon the quality of the copy submitted. Broken or indistinct print, colored or poor quality illustrations and photographs, print bleedthrough, substandard margins, and improper alignment can adversely affect reproduction.

In the unlikely event that the author did not send UMI a complete manuscript and there are missing pages, these will be noted. Also, if unauthorized copyright material had to be removed, a note will indicate the deletion.

Oversize materials (e.g., maps, drawings, charts) are reproduced by sectioning the original, beginning at the upper left-hand corner and continuing from left to right in equal sections with small overlaps.

Photographs included in the original manuscript have been reproduced xerographically in this copy. Higher quality 6" x 9" black and white photographic prints are available for any photographs or illustrations appearing in this copy for an additional charge. Contact UMI directly to order.

Bell & Howell Information and Learning
300 North Zeeb Road, Ann Arbor, MI 48106-1346 USA
800-521-0600

UMI®

POOL-BOILING ENHANCEMENT AND LIQUID CHOKING LIMITS WITHIN AND ABOVE A MODULATED POROUS-LAYER COATING

by

Scott Gayton Liter

A dissertation submitted in partial fulfillment
of the requirements for the degree of
Doctor of Philosophy
(Mechanical Engineering)
in The University of Michigan
2000

Doctoral Committee:

Professor Massoud Kaviany, Chairperson
Professor Gerard M. Faeth
Professor Herman Merte Jr.
Professor Wen-Jei Yang

ABSTRACT

Modulated (periodically non-uniform thickness) porous-layer coatings, as an example of capillary artery-evaporator systems, are experimentally shown to enhance the pool-boiling critical heat flux nearly three times over that of a plain surface, while maintaining low surface superheats. This enhancement is examined experimentally and discussed theoretically. This work marks the first such study on the effect of modulation of a porous-layer coating on pool boiling.

The fabrication of the modulated porous-layer coating consisting of sintered, monosized, spherical copper particles is described. Measurements of the heat flux versus surface superheat, during the wetted-surface regime and up to the critical heat flux, are presented for plain surfaces and surfaces with uniform and modulated porous-layer coating.

The modulation separates the liquid and vapor phases, thus reducing the liquid-vapor counterflow resistance adjacent to the surface. Theories are suggested for two independent mechanisms that are capable of causing the liquid-choking that leads to the critical heat flux. The liquid-choking limit predicted to occur first, with increasing surface heat flux, is considered to correspond to the critical heat flux experienced by the surface.

The Zuber hydrodynamic theory for the critical heat flux is modified to account for the effect of the coating modulation-wavelength on the development of a stable vapor layer above the coated surface, effectively choking the liquid down-flow to-

wards the surface (above the coating). The resulting hydrodynamic model relates this second liquid-choking limit to the inverse of the square root of the modulation wavelength. A finite-volume model of the transport in the porous-layer coating is used to predict the heat flux versus surface superheat. The second liquid-choking limit is predicted by this model and occurs within the porous-layer coating when the viscous drag surpasses the available capillary pumping.

The predicted wetted-surface regime and the two liquid-choking limits are compared with the measurements and good agreement is found. All of the tested surfaces are predicted to have hydrodynamically determined heat fluxes. The theories are then used to discuss the optimization of the enhancement and suggest that completely separated liquid and vapor flow paths can result in substantial further enhancement.

To my parents, Melvin and Cherry Liter.

ACKNOWLEDGEMENTS

I would like to thank everyone who has contributed to making my Ph.D. experience the most it could be. I would first like to praise my Lord and Father for not losing sight of me as I at times directed my focus to my studies. I also want to thank my parents, Melvin and Cherry Liter, for their unending and ever-ready support, encouragement, guidance, and example in every part of my life. I love them dearly and owe in large part any success I might ever gain to their efforts in my life.

I would also like to extend my deepest personal gratitude to Professor Massoud Kaviany for the father-like care and interest he has shown in me and my future. I wish I could communicate how much I value his sharing with me his ideas, philosophy, and excitement in regards to his personal and professional life. He has been an excellent teacher-of-life, a valued professorial role model, and a friend.

I give my sincerest thanks, as well, to my committee members, Professor Gerard Faeth, Professor Herman Merte Jr., and Professor Wen-Jei Yang for their time, service, comments, and interest in evaluating my doctoral work. Their own examples as researchers and educators has been an inspiration to me. I would also like to extend a personal thank you to Professor Majid Keyhani, my Master's advisor at the University of Tennessee, for his friendship and professional guidance, direction, and training.

The financial support I received from the General Motors Corporation, the Mechanical Engineering and Applied Mechanics Department of the University of

Michigan, and the National Science Foundation is appreciated.

My thanks also goes to the undergraduate students who have helped me on this project, Gregory Huff, Matthew Memmer, Andrew J. Mikloiche, Sotirios, and Brian Vivio. To the friends and colleagues I have had the priviledge to know in the porous media laboratory, David Burgess, Jae-Dong Chung, Mahmood Fatehi, Ozgur Karagozoglu, Leslie B. King, Justin MacLaurin, Minas Mezedur, Chan-Woo Park, and Timothy Purwin. And to the other friends I have made here in Ann Arbor, especially, Darryl Taylor, Paul Tortora, and Vincent Hahn. I would also like to thank my friends that encouraged me, often unknowingly, when I first came to Ann Arbor from Knoxville, and now again during the last few months, including the Elledge family, the Bowman family, David Brickner, Bruce Landis, and especially the very special love in my life, Amanda Gutwein. I could not imagine a more supportive and loving life-partner than her.

And finally, I would like to specifically thank Amir Oliveira, a fellow researcher from the porous media lab. He served me well for four years as a best friend and a mentor. His support, encouragement, professional and personal insights, and humor were indescribably helpful and appreciated. I do not think I would have finished without him.

TABLE OF CONTENTS

LIST OF FIGURES

LIST OF TABLES

Table

NOMENCLATURE

a	area ratio
A	area (m^2)
Bo	Bond number, $Bo_d = g\rho_l d^2/\sigma$
c_p	specific heat at constant pressure (J/kg-K)
C	constant
Ca	capillary number
C_E	Ergun coefficient
d	diameter (m)
$T_s - T_{lg}$	surface superheat (K or °C)
Δh_{lg}	enthalpy of vaporization (J/kg)
f	bubble departure frequency (1/s)
FSM	fluid side model
g	gravitational acceleration (m/s^2)
h	enthalpy (J/kg)
H	capillary rise height (m)
i	axial node counter
j	radial node counter
J	Leverett J-function, $J = J(s)$
Ja	Jakob number, Ja= $c_{p,l}(T_s - T_{lg})/\Delta h_{lg}$

k	thermal conductivity (W/m-K)
K	absolute permeability tensor (m^2)
ℓ	characteristic thermal-diffusion material thickness (m)
M	molecular weight (kg/kmol)
N	size of computational domain ($N \times N$)
p	pressure (Pa)
Pe	Peclet number, $\mathrm{Pe}_d = \langle u_l \rangle d/\alpha_l$
q	heat flux (W/m^2)
Q	heat transfer (W)
r	spatial coordinate, or radius (m)
R	base radius; or radius of curvature (m); or universal gas constant (J/kmol-K)
Re	Reynolds number, $\mathrm{Re}_d = (\rho_l \langle u_l \rangle d)/(\mu_l(1-\epsilon))$
s	saturation
SSM	surface side model
T	temperature (K)
u	velocity; or axial velocity (m/s)
U	uncertainty
v	radial velocity (m/s)
We	Weber number, $\mathrm{We}_{K^{1/2}} = (\rho_l \langle u_l \rangle^2 K^{1/2}) C_E \delta_s)/(\sigma C_J (K\epsilon)^{1/2})$
x	spatial coordinate; or length (m)
Z	Melrose function, $Z = Z(\theta_c)$

Greek symbols

α	thermal diffusivity (m^2/s)
δ	coating thickness (m)

δ_{ml}	macrolayer thickness (m)
ϵ	porosity; or area fraction
λ	flow-critical length scale; or wavelength (m)
μ	dynamic viscosity (kg/m-s)
ρ	density (kg/m^3)
σ	surface tension (N/m)
θ	included cone angle (degrees)
θ_c	contact angle (degrees)
τ	bubble departure time (s)

Subscripts

b	base layer; or base of characteristic hydrodynamic cell; or bubble
br	breakthrough
c	most critical λ_{RT}; or curvature; or capillary
cf	counter flow
CHF	critical heat flux
d	based on particle diameter; or most dangerous λ_{RT}
f	flow corridor
g	gas (vapor); or gas flow
h	hydrodynamic limit
i	axial node counter
j	radial node counter
$j_{e,i}$	last node of row i, $j_{e,i} = N - i + 1$
$j_{o,i}$	first node of flow corridor in row i, $j_{o,i} = i_s - i + 1$
J	Leverett coefficient

k	conduction
ku	conduction-convection
KH	Kelvin-Helmholtz
l	liquid
lg	liquid-vapor; or saturation
m	modulation
ml	macrolayer
o	outer radius, i.e., model domain boundary
p	plain (i.e., uncoated) surface
R	Rayleigh; or critical radius
RT	Rayleigh-Taylor
s	solid; or surface; or stack
v	viscous-drag limit
u	uniform porous-layer coating
Z	Zuber correlation for q_{CHF}

Superscripts

d	dispersion

Symbols

*	non-dimensionalized
$\langle\ \rangle$	volume or space averaged
$\parallel$	parallel to liquid velocity vector
$\perp$	perpendicular to liquid velocity vector

CHAPTER I

INTRODUCTION

1.1 Motivation

The efficiency and performance of devices experiencing high heat loads is often limited by the relationship between the generation or storage of heat in the device and the associated elevated and often undesirable device material temperatures. Examples of such limitations can be found in electronic cooling [1, 2], the increasing of the efficiency of process and heat transfer equipment, among others [3, 4, 5]. Future technologies promise ever higher heat loads and compels the search for improved heat transfer systems. The aim of this work is to examine the modulated (i.e., periodic variations of thickness) porous-layer coating of a boiling surface as a proposed means of enhancing surface heat transfer.

1.2 Introduction

Liquid-vapor phase change is a well recognized means for passively removing high heat loads from a device while maintaining relatively low material temperatures. A variety of processes and devices utilizing phase change have been explored to achieve this high heat load removal, including impinging-spray droplet evaporation [6, 7], thin film evaporation [8], heat pipes [9, 10, 11], and pool and flow boiling heat

transfer [12, 4, 5].

In the case of pool boiling, the critical heat flux q_{CHF} can be considered as the upper limit of the nucleate-boiling (or wetted-surface regime) heat flux from a surface. It occurs near the operating flux in which the vapor is generated at the rate of maximum vapor removal from the vicinity of the surface, beyond which flux the accumulating vapor would choke the liquid flow towards the surface. It marks the end of efficient cooling conditions near the surface, and in the case of a heat-dissipation controlled process, it marks the point of a runaway surface-temperature transient to the next stable operating point in the film boiling regime, qualitatively shown in Fig. 1.1 by the dashed arrow. The resulting temperature rise can be one to two orders in magnitude leading to surface dryout and, in many cases, device destruction or meltdown. Thus, the development of heat-dissipating, powered technology that utilizes nucleate boiling processes is limited by the q_{CHF}. Bergles [13] goes so far as to declare the q_{CHF} point as the most important design parameter of fixed-heat-dissipation devices. Despite nearly seven decades of dedicated examination that have generated vast amounts of experimental and theoretical research, there is still no general, clear consensus for the governing mechanisms of the q_{CHF} because of the many parameters influencing the vapor generation and removal processes.

Various surface modifications have been experimentally shown to passively provide effective enhancement of boiling heat transfer [4, 5]. The enhancement can be realized either as an increase in the q_{CHF}, or as a decrease in the surface superheat for a given heat flux q. This is schematically shown in Fig. 1.2. The surface superheat is defined here as the area-averaged solid surface temperature T_s beneath the porous-layer coating minus the fluid saturation temperature, i.e., $T_s - T_{lg}$.

Two classes of enhancing surface modifications that have proven to be com-

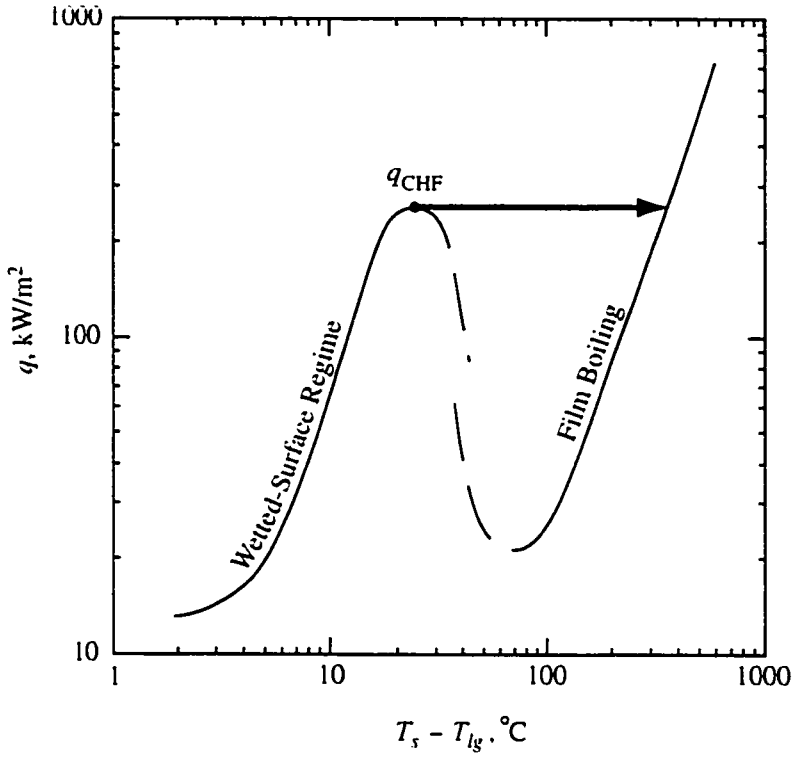

Figure 1.1: Typical boiling curve showing the different boiling regimes, q_{CHF}, and possible runaway surface-temperature transient for a heat flux controlled system.

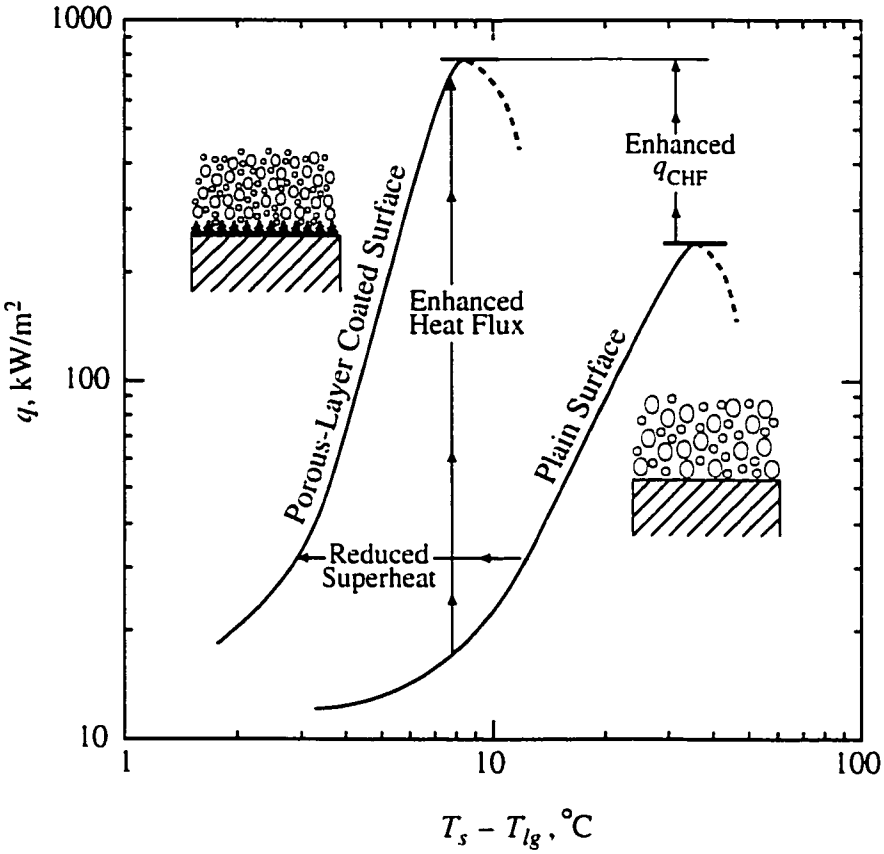

Figure 1.2: Schematic showing qualitative enhancement in the q_{CHF} and reduction in the $T_s - T_{lg}$.

Table 1.1: The q_{CHF} ratios of some commercial tubes with enhanced surfaces to a smooth tube [4].

Surface	$(q_{CHF})_{enhanced}/(q_{CHF})_{smooth}$
ECR-40	1.4
Gewa-T	1.5
Thermoexcel-E	1.5
High Flux	2.0

mercially viable, especially when applied to tubes, include integrated surface structures, such as channels and fins (e.g., the Furukawa Electric Everfin ECR-40, the Wieland-Werke Gewa-T, and the Hitachi Thermoexcel-E), and the application of a porous-layer coating to the surface (e.g., the Union Carbide High Flux). Table 1.1 presents enhancement ratios for these surfaces over that of smooth tubes as measured by Yilmaz and Westwater [4].

Figure 1.3 presents a map of the potential enhancement of the surface modifications as collected from the published experimental data. The enhancement zones shown are considered approximate and are generated from published data for various surfaces and geometries [4, 5, 14, 15, 16, 17], experimental results presented here (e.g., $q_{CHF}/q_{CHF,p} = 3$), and the expectations of the author.

Thin uniform thickness porous-layer coating of boiling surfaces has experimentally proven to be an especially effective passive enhancement technique capable of providing an increase in the critical heat flux q_{CHF}, and/or a reduction in the surface superheat $T_s - T_{lg}$ for a given surface heat flux q, compared to the performance of a plain surface [14, 15, 16, 17, 18, 19, 20, 21, 22]. In addition, a review of the q_{CHF} from an impermeable heated surface in contact with a thick porous medium is given

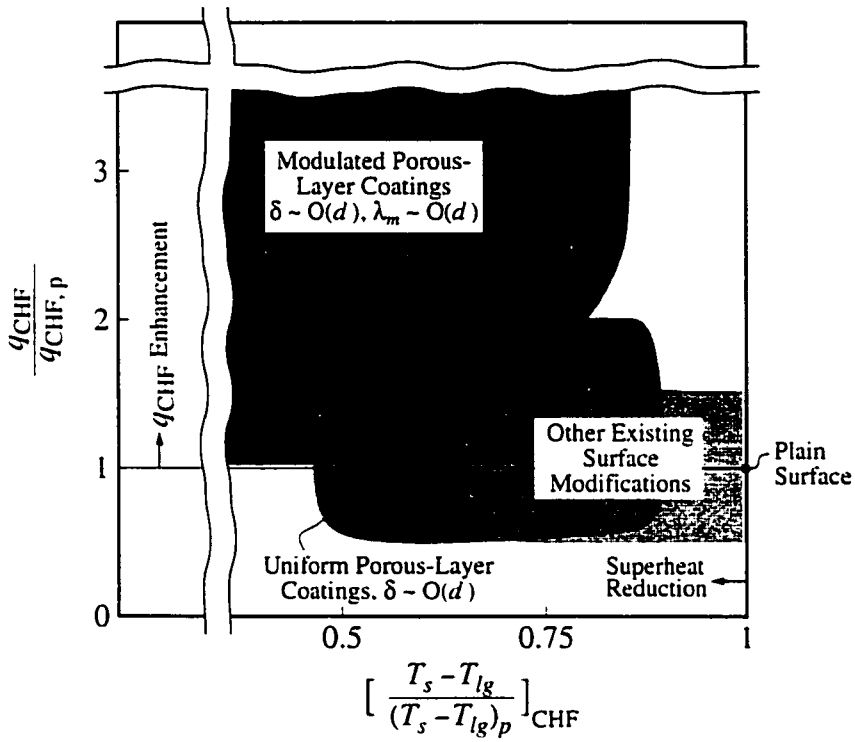

Figure 1.3: The potential of various surface modifications used to enhance pool boiling.

by Kaviany [23]. This review notes that a thick porous-layer coating would actually decrease the q_{CHF} by trapping the vapor inside the coating.

The use of porous layer coating to enhance the evaporation rate (i.e., q_{CHF}) is an example of a more general class of thermal systems utilizing a liquid-supply artery to feed an evaporation zone. Here, the heat transfer systems in this class are called capillary artery-evaporator systems. A well-known example of this class is the evaporator section of the heat pipe. A simple heat pipe can be viewed as a closed liquid-vapor phase-change system contained within a pipe with closed ends. In a section at one end of the pipe, vapor is condensed (i.e., heat is removed through the pipe wall in a region defining a condensation zone) and the condensed liquid is then drawn by capillarity and gravity through a wick to a section at the other end of the pipe to be evaporated (heat is added through the pipe wall in a region defining an evaporation zone). The generated vapor then flows from the evaporation zone through vapor channels running parallel to the wick and back to the condensation zone. There are a number of derived maximum heat flux limits bounding the operational range of a heat pipe including the viscous limit, the sonic limit, the entrainment limit, and the wicking limit [24]. These limits generally are formulated for cases in which the liquid draw is perpendicular to the applied heat flux in the evaporation zone (i.e., drawn axially through a wick in the pipe with radial heat addition), and they often include the effect of the geometry of the pipe from the evaporation zone to the condensation zone. This work focuses narrowly on the limits of the liquid and vapor flows to and from the evaporation interface as they relate to the q_{CHF} and the q versus $T_s - T_{lg}$ curve, and does not address the vapor flow after it leaves the evaporation zone, nor does it address the condensation zone. The operating limits developed to describe heat pipes then are not explicitly discussed in

this work, but instead specific upper limits for the heat flux (i.e., liquid-choking) are developed for the capillary artery-evaporator systems.

Therefore, the focus of this work is on relatively thin porous-layer coatings with structural modulations (i.e., spatially periodic variations of layer thickness) that encourage preferential liquid and vapor counterflow paths entering and exiting the coating, which in turn facilitate the vapor flow away from the surface, delaying surface dryout and allowing sustained higher heat fluxes.

1.3 Modulated Porous-Layer Coatings

Modulated porous-layer coatings are coatings with periodic, designed variations of layer thickness δ. The modulation is imposed to create alternating regions of low resistance to vapor escape and high capillary-assisted liquid draw. This would result in the preferential liquid-vapor counterflow paths within the layer facilitating heat transfer from the surface to the liquid pool in a manner similar to that of thermosyphons (i.e., heat pipes).

Figures 1.4 and 1.5 show micrographs of example modulated porous-layer coatings. A description of the fabrication of these coatings is given in Chapter 3.

1.4 Background

In boiling from high conpacitance [i.e., an effective surface material thickness ℓ multiplied by the surface material effusivity $(\rho c_p k)_s^{1/2}$] plain (uncoated) surfaces, the resistance to liquid flow towards the surface can be considered to arise from the thermal-hydraulics in the liquid-vapor counter-flow directly above the surface and in the liquid pool. Zuber [25] theorized for infinite plain surfaces that the hydrodynamics impose stability limits to the counterflow determining a hydrodynamic

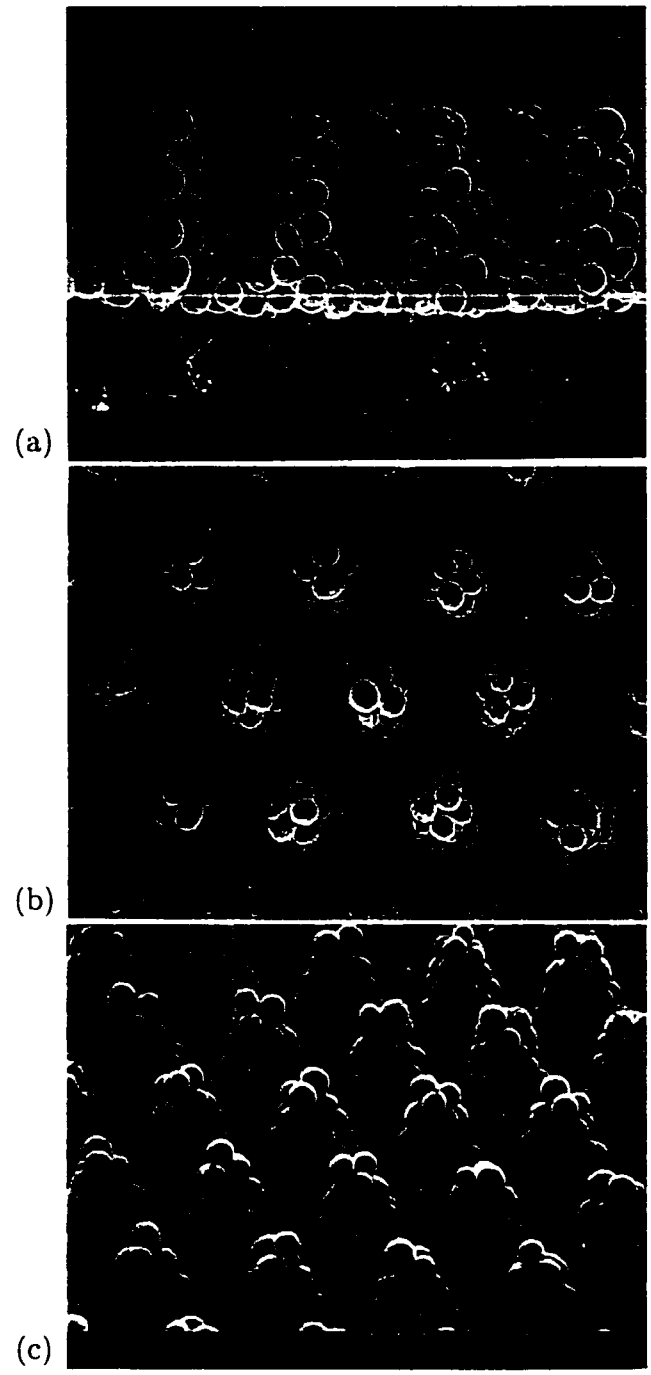

Figure 1.4: SEM of single-height, modulated porous-layer coating showing (a) the side view, (b) top view, and (c) the perspective view. The porous-layer contains spherical copper particles of diameter $d = 200$ μm molded into conical stacks.

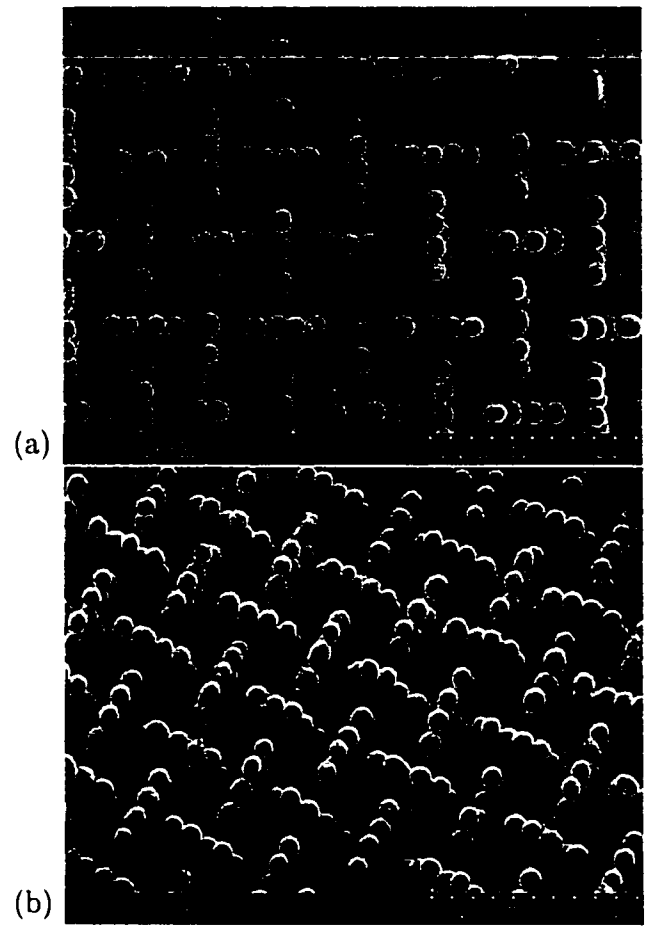

Figure 1.5: SEM of single-height, modulated porous-layer coating showing (a) top view, and (b) the perspective view. The porous-layer contains spherical copper particles of diameter $d = 200$ μm molded into tapered walls.

liquid-choking limit (i.e., critical heat flux $q_{CHF,Z} = q_{CHF,p}$).

In boiling from thick porous layers, there is an additional resistance to the liquid-vapor counterflow imposed by the solid porous matrix that can act to "trap" the escaping vapor above the phase-change interface and within the layer, thus reducing the relative permeability of the liquid and causing a viscous-drag determined dryout at fluxes much lower than that of plain surfaces (i.e., $q_{CHF,v} \leq q_{CHF,p}$) [23, 26]. Udell [26] derived an expression for the critical heat flux of a deep porous layer with internal liquid-vapor counterflow, $q_{CHF,cf}$, as

$$\frac{q_{CHF,cf}}{\frac{K\rho_g \Delta h_{lg} g(\rho_l - \rho_g)}{\mu_g}[1 + (\frac{\rho_l \mu_g}{\rho_g \mu_l})^{1/4}]^{-4}} = 1. \tag{1.1}$$

Thin layers, however, when not thick enough to appreciably resist vapor escape, have been shown to enhance the critical heat flux (i.e., $q_{CHF,v} \geq q_{CHF,p}$) [15, 16, 20, 27, 28]. This enhancement is believed to be due to the lateral capillary-assist to the liquid-flow towards the phase-change interface, which reduces the liquid-vapor counter-flow resistance (i.e., provides preferential flow paths for the liquid and vapor, or phase separation), and prolongs the liquid-"wetting" of the solid material. The porous layer also creates non-hydrodynamically determined locations of vapor escape into the liquid pool possibly altering the thermal-hydraulics and extending the hydrodynamic liquid-choking limit (i.e., $q_{CHF,h} > q_{CHF,Z}$) [21, 28].

A number of phenomenological theories have been put forth to explain boiling heat transfer from porous-layer coatings. This enhancement is attributed to combinations of an extended surface area effect, a capillary-assist to liquid flow effect, an increased nucleation site density effect, and the dependence of the vapor escape paths from the porous-layer on the pore distribution at the top of the layer adjacent

to the liquid pool. These effects are dependent on the fluid and solid thermophysical properties and geometrical coating parameters, such as coating thickness δ and pore size distribution. The exact relational dependence is not well understood and the extent of possible enhancement is not known. Due to the complexity of the flow conditions and phase-change processes inside and near the porous coating, analytical models have not been developed that have proven to be applicable over a wide range of the physical parameters without the use of several empirical constants.

1.4.1 Critical Heat Flux Modeling

In a general sense, the limit on the q_{CHF} of any evaporating (e.g., pool boiling) system depends on the mechanisms of liquid supply to and vapor escape from the phase-change interface, and therefore can be considered to be limited by the liquid and vapor flow resistances. The theoretical maximum would then be the kinetic limit for the resistance to the evaporated vapor molecules leaving the liquid-vapor interface, or that described by Gambill and Lienhard [29] as the kinetic limit for evaporation given by

$$q_{\text{CHF,max}} = \left(\frac{R_g}{2\pi M}\right)^{1/2} \Delta h_{lg}(p_g)[\rho_g(p_g)T_{lg}^{1/2}(p_g) - \rho_{g,\infty}T_{lg,\infty}^{1/2}], \tag{1.2}$$

where ρ_g, T_{lg}, and Δh_{lg} are functions of the local vapor pressure at the liquid-vapor interface, and where subscript "∞" denotes a far-field pressure (here assumed to be $p_g = 1$ atm). The interface p_g is higher than the far-field pressure to enable the flow of evaporated molecules leaving from the interface (due to heat addition). As an example, this results in $q_{\text{CHF,max}} = 8.09 \times 10^7$ W/m^2 for pentane evaporating to a vacuum. In practice, achievable, passively enhanced and sustainable q_{CHF} are smaller by two orders of magnitude. But this shows that there is much room for

enhancement.

Within the liquid pool above the surface, and to a certain extent within porous layers of uniform layer thickness, the liquid supply and vapor escape occur as a liquid-vapor counterflow resisting each others motion. As the heat flux is increased, the liquid flow rate supplying the resulting evaporation, and in turn the liquid flow resistance, must increase. Eventually, a q_{CHF} is reached where either the liquid flow towards the phase-change interface chokes as in the case for high effusivity surfaces [i.e., high $(\rho c_p k)_s^{1/2}$ surface and coating materials capable of maintaining a nearly uniform temperature], or the phase-change interface is reduced due to the development of local material hot spots above a critical rewetting temperature (local dryout locations) as in the case for low effusivity surfaces. This work restricts itself to cases where the surface and coating materials are both assumed to exhibit high conpacitance.

From an examination of the literature, various approaches have emerged that describe the way the q_{CHF} is viewed and modeled. Here, these approaches are classified into two broad categories: Fluid-Side Models (FSMs) dealing with the hydrodynamics just above the surface, and Surface-Side Models (SSMs) dealing with effects of surface characteristics and material properties.

1.4.1.1 Fluid-Side Models

The term fluid-side model (hereafter, FSM) refers to those models that are governed by the thermo-hydraulics and hydrodynamics just above the surface on which boiling occurs. FSMs, in general, are independent of the surface characteristics and material. These models assume the formation of effective, liquid-vapor structures or patterns, mechanistically idealizing the liquid and vapor flow paths above the

surface. The q_{CHF} is then said to occur when some criterion, as a function of the heat flux and idealized liquid-vapor counterflow structure, is achieved causing vapor-binding. Vapor-binding refers to the choking of the liquid, or rather, the inability of the liquid to wet the surface by penetrating through the vapor generated at the surface. This criterion can take various forms, such as the onset of a liquid-vapor interfacial instability, some form of a time scale relating to bubble dynamics, or a critical bubble-packing density over the surface which produces bubble coalescence. Three main FSM classes can be defined by these three criteria, namely the single-staged hydrodynamic model class, the multi-staged hydrodynamic model class, and the bubble coalescence model class. After a brief review of some hydrodynamic basics common to many of these models, these classes are discussed below.

Hydrodynamic Basics: Single-staged and multi-staged hydrodynamic models are so named for their basis in linear hydrodynamic stability theory. In particular, they rely heavily on the Kelvin-Helmholtz and the Rayleigh-Taylor interfacial stability wavelengths, given respectively as

$$\lambda_{KH} = \frac{2\pi\sigma}{\rho_g u_g^2} \tag{1.3}$$

and

$$\lambda_{RT} = C_1 2\pi\left[\frac{\sigma}{g(\rho_l - \rho_g)}\right]^{1/2}. \tag{1.4}$$

where C_1 in Eq. (1.4) equals unity for the most critical wavelength $\lambda_{RT,c}$, and $C_1 = 3^{1/2}$ for the "most dangerous" (i.e., fastest growing) wavelength $\lambda_{RT,d}$. These models generally idealize and simplify the liquid-vapor counterflow above the surface as

consisting of vertical, vapor-escape columns surrounded by the liquid. These columns are used in the models either as the complete vapor-escape path, or as part of a vapor escape system, possibly as vapor conduits leaving the surface and terminating in a vapor mass (bubble).

The Kelvin-Helmholtz wavelength λ_{KH} describes the periodic interfacial shape that naturally arises due to physical instabilities resulting from a relative motion between two adjacent, different fluids in the absence of a body force. In this case, the λ_{KH} is related to the vertical interface between a liquid surrounding a vapor jet through which the generated vapor is escaping from the heated surface. The λ_{KH} determines the critical balance between surface tension working to stabilize the jet and the velocity-dependent, flow-induced pressure forces working to destabilize the jet. The manner in which these wavelengths are used in hydrodynamic models will be discussed later. This wavelength with the resulting interfacial pattern is shown conceptually in Fig. 1.6(a).

The Rayleigh-Taylor wavelength λ_{RT} describes the periodic interfacial shape that naturally arises due to physical instabilities inherent in the situation where an adverse density gradient exists parallel to a body force across the interface of two motionless fluids. The λ_{RT} determines the critical balance between surface tension working to stabilize the interface and buoyancy forces working to destabilize the interface. In this case, the λ_{RT} also indicates the locations along the interface between a vapor and a superpositioned liquid where the vapor will theoretically rise through and penetrate into the liquid due to gravitational forces (buoyancy). This wavelength with the resulting interfacial pattern is shown conceptually in Fig. 1.6 for an infinitely large, upward-facing, horizontal surface.

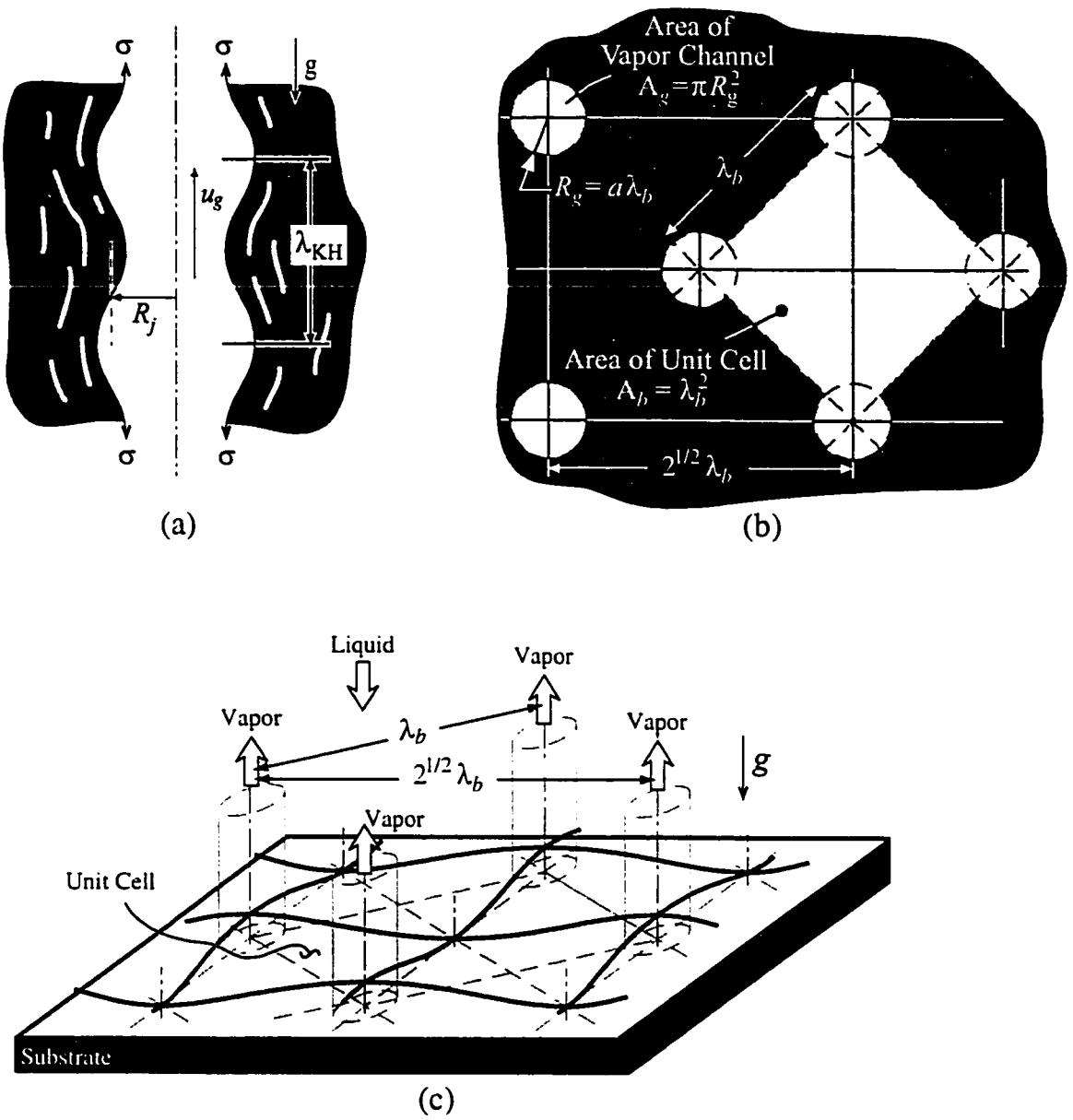

Figure 1.6: Conceptual schematics showing the λ_{KH} and the λ_{RT}. (a) The λ_{KH} associated with a vapor jet; and (b) top view and (c) perspective view of the resulting λ_{RT}-spaced array of locations of vapor rise into a superpositioned liquid on an infinitely large, upward-facing, horizontal surface. (Redrawn based on figures by Lienhard and Witte [30])

Single-Staged Hydrodynamic Models: The single-staged hydrodynamic class of models refers to those models for the q_{CHF} that assume a steady, time-independent, liquid-vapor structure above the surface. One of the more well-known versions of this class is the model proposed by Zuber and Tribus, in Zuber's doctoral thesis [25], where stable, vertical vapor jets are distributed in an array over a surface corresponding to the circles in Fig. 1.6. This model is expanded and used in the present work here, and therefore, a more detailed description is left until Chapter 2. Briefly, in this model, liquid flows towards the surface and evaporates. The vapor that is generated then escapes away from the surface through the circular vapor jets of a given radius $R = \lambda_{RT}/4$. As the heat flux is increased towards the q_{CHF}, the rate of vapor generation increases, and from mass continuity, the vapor velocity increases. The q_{CHF} is then achieved when the vapor velocity u_g becomes greater than the critical velocity for a circular jet into a fluid, as determined by the λ_{KH}.

Zuber then performed an energy balance between the heat flux at this critical velocity and the escaping latent heat associated with the vapor to eventually reach his well-known correlation for the critical heat flux:

$$q_{CHF,Z} = C_2 \rho_g^{1/2} \Delta h_{lg} [\sigma g(\rho_l - \rho_g)]^{1/4}, \tag{1.5}$$

where he recommends, as an approximation, $C_2 = (\pi/24)$, to approximate both choices of C_1 in Eq. (1.4).

Before the publication of Zuber's thesis, Kutateladze [32] presented a number of dimensionless groups describing the "flooding" of a distillation column. He then related these groups to boiling processes and scaled the critical heat flux with the "flooding" mechanism. This resulted in a dimensionless form similar to Eq. (1.5)

as [30, 31, 32]

$$\frac{q_{\mathrm{CHF}}}{\rho_g^{1/2}\Delta h_{lg}[\sigma \mathrm{g}(\rho_l - \rho_g)]^{1/4}} = C_3 \equiv \mathrm{Ku}. \tag{1.6}$$

Since this time, the left-hand-side of Eq. (1.6) has been referred to as the Kutateladze Number, Ku. Kutateladze then compared Eq. (1.6) with various experimental data and recommended a value for the constant of $C_3 = 0.131$, nearly identical to Zuber's constant of $C_2 = \pi/24 = 0.1309$ [31].

One common shortcoming of all the single-staged hydrodynamic models is the need to specify, or assume, a value for the λ_{KH}. Lienhard and Hasan [33] presented one method of replacing this need with that of knowing the surface area of departing bubbles by utilizing a mechanical energy stability criterion. They equate the rate of kinetic energy increase due to the flow of generated vapor into a growing, hovering vapor mass to the release of capillary energy per unit volume resulting from bubble departure. By doing so, they are able to specify the critical u_g. This method, though more complicated in its formulation and application, becomes useful when assumptions about the λ_{KH} become difficult to make.

For their highly idealized simplicity, single-staged hydrodynamic models have enjoyed remarkable success in predicting the q_{CHF}, especially for highly wetting fluids. The physical model of stable, large-scale vapor columns, however, does not resemble photographic evidence of the boiling process at high heat fluxes. Multi-staged models have therefore been developed towards finding a more physically-true, and generally applicable, hydrodynamic description of the q_{CHF}.

Multi-Staged Hydrodynamic Models: The multi-staged hydrodynamic class of models refers to those models for q_{CHF} that assume a quasi-steady, often time-

dependent, liquid-vapor structure and cyclic pattern above the surface. One of the more well-known versions of this class is the model proposed by Haramura and Katto [34] in which the structure takes the idealized form of that shown in Fig. 1.7. Again, for lack of a better assumption, the unit cell for heat transfer in the Haramura-Katto model is the same as that shown in Fig. 1.6. Based on photographic studies, this model assumes the existence of a thin macrolayer on the heater surface consisting of a liquid film transversed by many small, vertical vapor passages. Conceptually, this model determines the q_{CHF} by relating the time for macrolayer evaporation to the vapor bubble dynamics. More precisely, a vapor mass is assumed to hover at the top of the macrolayer while being supplied with additional vapor from the macrolayer evaporation. After a calculable period of time, the vapor mass departs as a bubble, allowing immediate replenishing of the macrolayer to its maximum, initial thickness, δ_{ml}.

Haramura and Katto noted that in the photographic studies they reviewed, the δ_{ml} was reported to be inversely related to the heat flux. The criterion for the q_{CHF} in their model is therefore prescribed as the balance between the bubble departure time τ (also referred to as the hovering period) and the time necessary to evaporate a macrolayer of a critical thickness $\delta_{ml,c}$ corresponding to the q_{CHF}. The critical thickness was related to the λ_{KH}. They used their resulting correlation to predict, with fair results, the q_{CHF} for a variety of boiling conditions, from pool boiling on cylinders and small disks without sidewalls, to even some flow boiling situations.

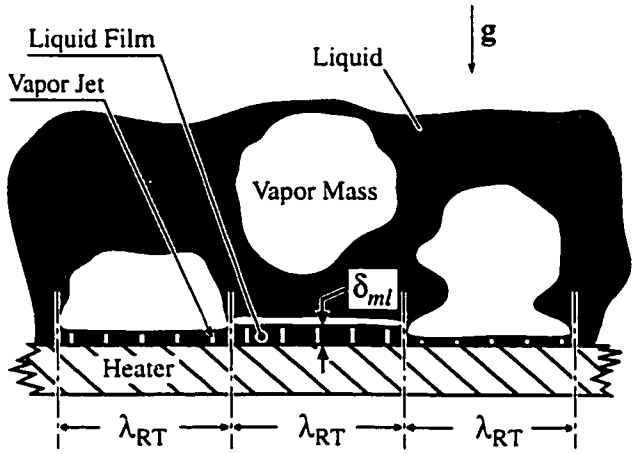

Figure 1.7: Conceptual schematic showing the liquid-vapor jet structure in the Haramura-Katto multi-staged hydrodynamic FSM. (Redrawn based on a figure by Haramura and Katto [34])

Bubble Coalescence: Although both multi-staged and single-staged hydrodynamic models have exhibited fair success in predicting the q_{CHF}, they still have many shortcomings and are suffering in their acceptance to what is becoming a more and more limited applicability as the development of powered technology advances. To explain, hydrodynamic models were developed independently of surface characteristics and therefore, in their current state, do not consider such factors affecting the q_{CHF} as bubble-size scale structures on the surface, the surface material effusivity (i.e., $(\rho c_p k)_s^{1/2}$), and the contact angle along triple-phase lines on the surface (i.e., the wettability). Hydrodynamic models are tailored to situations in which these effects are minimized, such as boiling of highly wetting liquids on high conductivity, thick heaters with nearly smooth surfaces. As such, these models can be considered as providing upper limits for the range of the q_{CHF} from nearly smooth surfaces, since high contact angles and thin heaters tend to lower the q_{CHF}.

Before the generation of the first hydrodynamic models, attempts were made to model the q_{CHF} based on some observations of the surface. These observations, however, were mainly used to determine the distribution of vapor generating sites (nucleating sites), which in turn was used to determine bubble locations and the bubble-packing density distribution over the surface. Once the bubble locations were determined, the mechanism for the q_{CHF} was considered to be bubble crowding, or bubble coalescence, over the surface causing vapor-binding, and thus are classifiable here as FSMs.

One of the first reported model of this type was suggested by Addoms as reported by Rohsenhow and Griffith [35]. He assumed a system in which bubble packing in a square array on a surface would lead to liquid choking. He used dimensional analysis to relate an average vapor velocity scaled with an effective thermally

diffusive-buoyant liquid velocity to a pressure effect in the form of a buoyancy term. His resulting relation is [35]

$$\frac{q_{\mathrm{CHF}}}{\rho_g \Delta h_{lg} (\alpha_l \mathrm{g})^{1/3}} \sim \frac{\rho_l - \rho_g}{\rho_g}. \tag{1.7}$$

Equation (1.7) was then revised by Rohsenow and Griffith [35], who, citing an observation that the rise-speed of bubbles appears to be "very fast," assumed gravity had a negligible effect on q_{CHF}. They, instead, postulated a q_{CHF} criterion in which the average vapor velocity would scale with the bubble detachment velocity fd_b resulting in

$$\frac{q_{\mathrm{CHF}}}{\rho_g \Delta h_{lg} (f d_b)} \sim \frac{\rho_l - \rho_g}{\rho_g}. \tag{1.8}$$

Rohsenhow and Griffith [35], citing experiments by Jakob that found the fd_b for boiling of CCl_4 and H_2O was nearly constant (at 0.078 m/s), curve fit some experimental data to obtain the following dimensional relation

$$\frac{q_{\mathrm{CHF}}}{\rho_g \Delta h_{lv}} = 0.012 \left(\frac{\rho_l - \rho_g}{\rho_g}\right)^{0.6}. \tag{1.9}$$

These models have not garnered wide acceptance due to the difficulties in predicting f and d_b. Other models that are similar to, or have evolved from Addom's [35] mechanistic model are still being studied today in which two-phase flow near the surface is being modeled using integral momentum, energy, and interfacial density balances [36]. But these models, as with the hydrodynamic models, remain detached from surface material effects. However, a number of researchers have used

the bubble coalescence model's concept of using nucleation sites in determining bubble spacing on the surface as inspiration for looking at ways to include the heater itself in modeling of the q_{CHF}.

1.4.1.2 Surface-Side Models

In attempts to explain over-predictions of q_{CHF} as a function of $T_s - T_{lg}$ from FSMs for thin heating surfaces, surfaces with low conpacitance (i.e., $\ell(\rho c_p k)_s^{1/2}$, a combination of parameters considered by some to correlate experimental surface-side effects on pool boiling [19, 37]), and fluid-surface combinations with large contact angles, a number of SSMs have been developed. These are similar to bubble coalescence models in that they look to nucleation sites to provide and define unit cells on the surface, but they are very different in the way they use these cells. The SSMs, like the bubble coalescence models, consider the nucleation site density on a surface to be dependent on the heat flux. They then consider the local effects on the unit cells, such as the local, distributed surface temperature profile, and the presence of a fluid microlayer underneath the bubble from which the majority of evaporation (i.e., solid to fluid heat transfer) takes place.

Concepts behind SSMs, then, include the theories of local hot-spots, or dry-spots, and their relationship to the surface characterization (e.g. nucleation site density, wettability, orientation) and the surface material effusivity [37, 38, 39, 41, 42, 43]. The concept of local hot-spots is related to the concept of conpacitance $[\ell(\rho c_p k)_s^{1/2}]$. The conpacitance is a measure of the relationship between a heater's ability to store energy and its ability to conduct it laterally along the surface. It was first suggested by Bar-Cohen, but no physical modelling was given as justification for its use as a correlating parameter [44]. The q_{CHF} has been shown to qualitatively

correlate with the conpacitance [37, 38, 41, 43, 44]. If a heater exhibits a relatively low conpacitance, then it may experience local areas of high temperature compared to the surface-averaged temperature. These high local temperatures can accelerate the evaporation of the microlayer underneath a bubble such that it becomes on the same order of time as the bubble departure frequency. The resulting dry-spot under the bubble can act as a local insulator driving the surface temperature up even higher. When these areas of high temperature exceed a critical rewetting temperature, then local dryout is said to occur, often spreading over the surface and leading to global q_{CHF} over the surface.

Other SSMs consider local surface temperatures and their effect in activating new nucleation sites and altering bubble departure frequencies. As the local temperatures are increased, local areas of higher nucleation site densities will develop. A critical packing of bubbles will then be reached in these areas of high site-density which can lead to a local dryout that, again, can spread over the surface leading to q_{CHF} [42].

Surface-side factors have been shown to have a strong influence on the q_{CHF}. The exact characterizations of the surface that govern this influence are uncertain, but they are believed to be strongly related to the material properties, fluid-solid wettability, and bubble departure frequency. As a result of this current uncertainty in the exact relationships between surface-side characteristics and the q_{CHF}, empirical correlation is widely used.

In the situations where the effects of surface-side characteristics are minimized, FSMs have exhibited fair success in predicting the q_{CHF}. Such situations include boiling from large surface areas, boiling from high effusivity surfaces, and boiling with highly wetting liquids. Since all of these situations appear to help main-

tain a wetted and even-temperatured surface, FSMs appear to provide an upper limit for the q_{CHF} from smooth surfaces.

This study restricts itself in scope to highly-wetting fluids boiling on high conpacitance surface and coating materials, therefore, further details regarding the SSMs in the sense described above are not presented here. Rather, an extension will be made of the single-stage hydrodynamic FSM that incorporates into the q_{CHF} model a functional dependence of the surface-side **geometry** characterizing the porous-layer coating (see Chapter 2). I.e., this dependence of the q_{CHF} on the surface-side geometry is considered independent of the material conpacitance.

1.5 Scope and Objective

The use of porous layer coating to enhance the evaporation rate (i.e., q_{CHF}) is an example of a capillary artery-evaporator system. The capillary pumping in the porous media generates the liquid draw thus establishing the fluid flow artery. By designing the artery in such a way as to provide controlled direction to the fluid flows and to reduce and minimize the liquid-vapor counterflow resistance (i.e., create phase separation with directed flow paths), significant enhancements in the sustainable heat loads can be achieved. This work endeavors to theoretically analyze and experimentally utilize such an artery-evaporator system. Specifically, the advantages of porous-layer coatings in pool boiling heat transfer are enhanced by the design of arteries within the porous layer that promote phase separation within the layer aimed at reducing the liquid-vapor counterflow resistance. These arteries are realized in the form of modulation of the porous-layer thickness. In the example of a modulated porous-layer coating presented in this work, the vapor escape is relegated to flow out of the layer from between the modulation peaks (i.e., not internally through the

porous medium). The liquid flows into the tip of the modulation peaks and towards the surface through the porous medium to the location where evaporation occurs. The local regions along the coating of larger porous-layer thickness then become the liquid-flow arteries.

More specifically, this work theoretically and experimentally analyzes the use of porous-layer coatings in pool boiling heat transfer while designing means to promote phase separation within the layer aimed at reducing the liquid-vapor counterflow resistance. The ultimate goal is to enhance the q_{CHF} and the q versus $T_s - T_{lg}$ curve for such surface-coating systems. This is to be done by implementing porous-layer macrostructures created by designed modulation of the layer thickness, thus providing the designed preferential vapor escape paths and liquid-flow arteries. To reduce the number of variable parameters, this study restricts itself to atmospheric pressure, 1-g, saturated pool boiling of pentane from flat horizontal (i.e., negligible lateral effect of buoyancy across the surface) copper surfaces with various modulated porous-layer coatings consisting of sintered, spherical copper particles with selected uniform diameters.

Below, the modulated porous-layer coating is described, followed by a theoretical approach to the prediction of the boiling performance of these coated surfaces, and then by a description of the experiments. Finally, the experimental results are presented, compared with the predictions, and discussed.

CHAPTER II

THEORY

2.1 Theoretical Approach

It is hypothesized that the modulation of the porous-layer coating separates the liquid and vapor phases to enable capillary assisted liquid feeding to an evaporation zone with minimal resistance to vapor escape, and that two possible mechanisms exist for the choking of the liquid flow towards the surface (i.e., the q_{CHF}); namely the hydrodynamic and viscous-drag liquid-dhoking limits.

In the fluid above the surface, there is a hydrodynamic liquid choking limit, $q_{\mathrm{CHF,h}}$, that can be mechanistically related to hydrodynamic instabilities as functions of flow-critical length scales and fluid properties. Here, this liquid-choking limit *above* the coating is characterized by

$$\frac{q_{\mathrm{CHF}}}{g\sigma\rho_g^2\Delta h_{lg}(\rho_l-\rho_g)} = f[\frac{g(\rho_l-\rho_g)\lambda_{\mathrm{RT}}^2}{\sigma}, \frac{\lambda_m}{\lambda_{\mathrm{RT},c}}, ...]. \tag{2.1}$$

where the ellipsis points would imply other parameters leading to dry-out limits, and λ_m is the modulation wavelength of the coating. Zuber [25] originally formulated this limit for a uniform-temperature plain surface (i.e., the coating thickness $\delta \rightarrow 0, q_{\mathrm{CHF,h}} \rightarrow q_{\mathrm{CHF,Z}}$). This hydrodynamic liquid-choking limit is dependent on the

fluid properties and the surface macro-scale geometry, but not the microscale surface characteristics or particle diameter, and therefore does not account for their effects. The hydrodynamic theory also is incapable of predicting the q versus $T_s - T_{lg}$ curve in the nucleate-boiling (wetted) regime.

Within a porous-layer coating, the counter flow of liquid and vapor can also result in a liquid-choking limit, $q_{\mathrm{CHF,v}}$, due to a critical viscous-drag resistance in the fluid. This viscous-drag liquid-choking limit is dependent on the fluid and coating material properties and the macro- and pore-scale geometries of the coating. Here, the liquid-choking limit of this model *within* the coating is characterized by

$$\frac{q_{\mathrm{CHF,v}}}{\frac{\rho_l \sigma \Delta h_{lg}}{\mu_l}} = f\left[\frac{\rho_l \langle u_l \rangle^2 K^{1/2}}{\sigma}, \frac{c_{p,l}(T_s - T_{lg})}{\Delta h_{lg}}, \frac{\langle u_l \rangle \mu_l}{\sigma}, \frac{\langle u_l \rangle d}{\alpha_l}, \frac{k_s}{k_l}, \frac{d}{\delta}, \frac{(K/\epsilon)^{1/2}}{d}, \ldots\right] \quad (2.2)$$

where d is the particle size, δ is the maximum layer thickness, ϵ is the porosity, K is the absolute permeability, and the ellipsis points again implies other parameters leading to dry-out.

The realized q_{CHF} on a surface would then correspond to the liquid-choking limit that first occurs, either above the coating due to the liquid-vapor counter-flow hydrodynamics, or within the coating due to the liquid-flow viscous drag. These limits in their functional form are shown in Fig. 2.1. Also shown is the kinetic limit for evaporation as presented in Chapter 1, and the hydrodynamic liquid-choking limit for surfaces porous-layer coating and the deep-layer counter-flow liquid-choking limit to be discussed later.

The modeling required to determine the $q_{\mathrm{CHF,v}}$ also enables the determination of the q versus $T_s - T_{lg}$ in the wetted-surface regime prior to reaching q_{CHF}. In the next section, the physical model and accompanying simplifying assumptions are presented

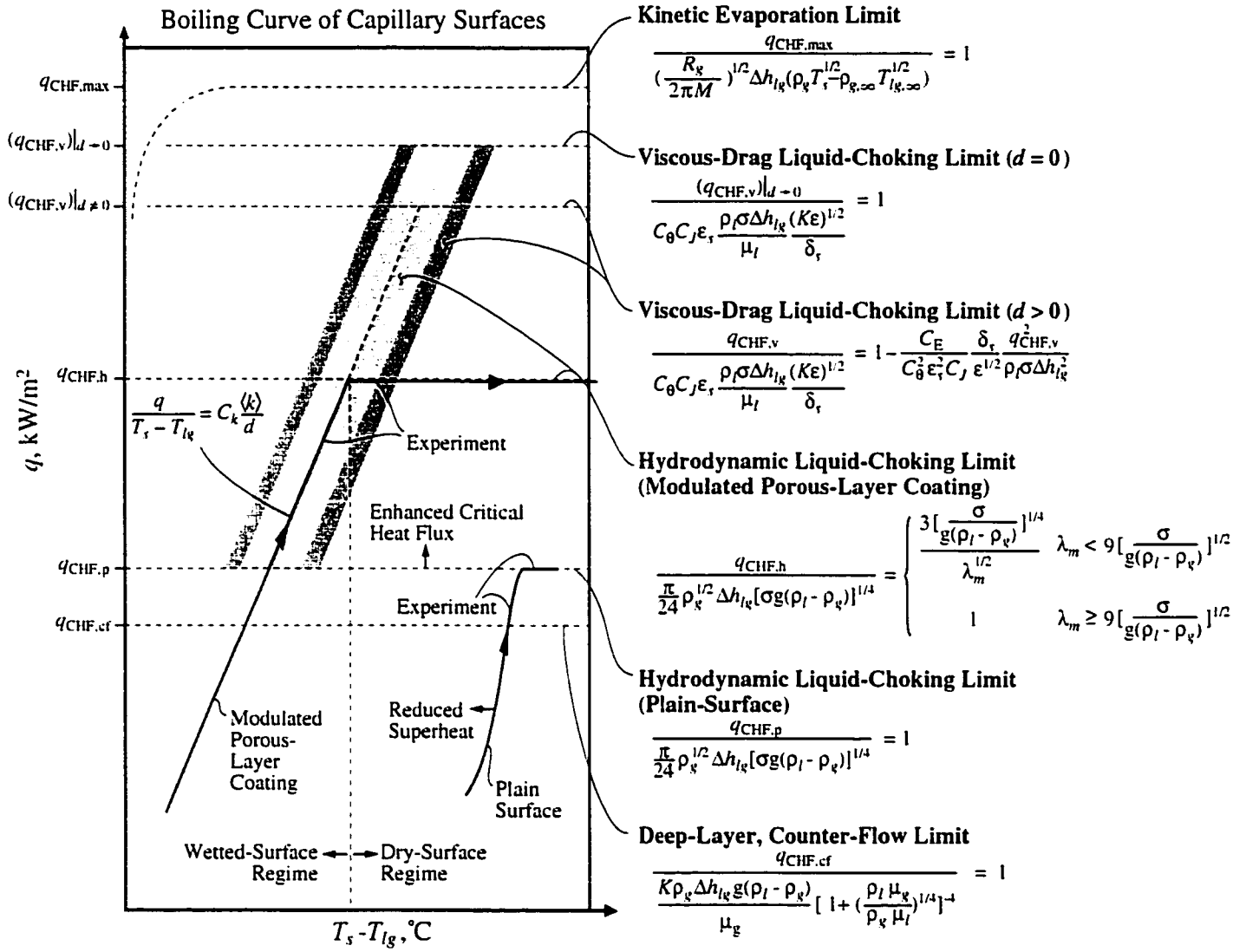

Figure 2.1: A rendering of the various regimes in pool boiling with modulated porous-layer coating.

and discussed, followed by the theory predicting the q versus $T_s - T_{lg}$, and then the descriptions of the two proposed liquid-choking mechanisms.

2.2 Liquid Flow and Heat Transfer Models

To describe, predict, and optimize the liquid flow within the porous-layer coating, the flow paths to an evaporation zone must be modeled. Valid simplification of the flow paths is difficult since the complex liquid-vapor counterflow during boiling from the thin, modulated porous-layer coating is not well understood. This lack of understanding is attributed to the small range of length scales and the difficulty of visually observing the phenomena. The additional non-homogeneity introduced by the modulation of the coating thickness further complicates the problem and makes valid simplification difficult. It is believed that a combination of point-wise, particle-level, and volume-averaged treatments are necessary to model the performance of such coatings. Here, some simplifying assumptions are made in regard to the flow paths, without rigorous validation, in order to develop a model that allows for initial, qualitative study of the q versus $T_s - T_{lg}$ curve and of the viscous-drag liquid-choking limit.

Figure 2.2 shows the proposed physical model for the liquid and vapor flow paths within and above a porous-layer coating with modulation in the form of conical particle stacks. This model is based on the geometry of the fabricated and experimentally tested surfaces. The stacks themselves is assumed to be porous media of uniform porosity and contained within axially symmetric frustums of right circular cones of height $\delta_s = \delta - d$ situated on top of a uniform base layer of single-particle thickness d. Local volume averaging of properties, temperature, and liquid velocity are assumed to be valid, without restriction and regardless of the particle-domain

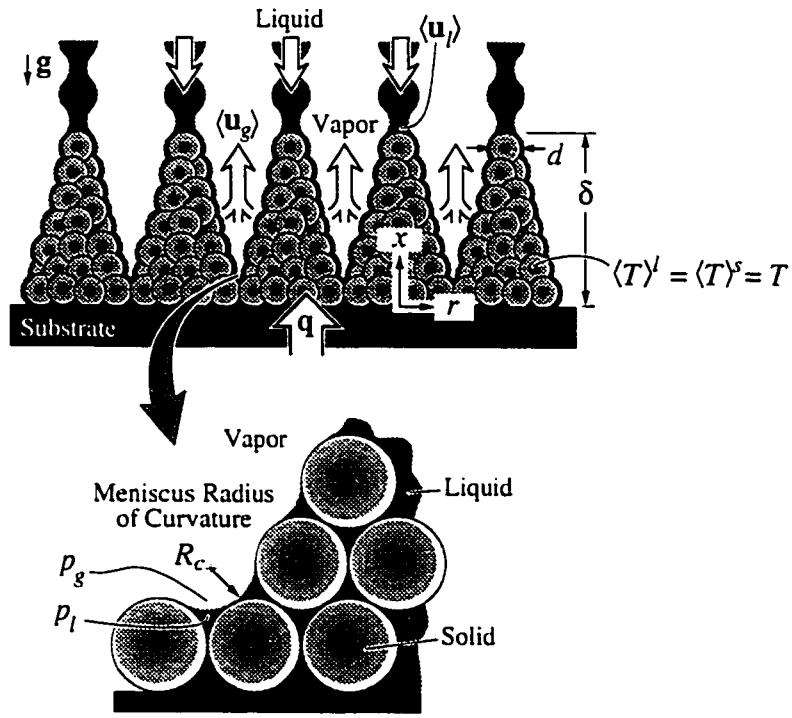

Figure 2.2: A rendering of the physical model of the viscous-drag instability limit to liquid reaching the surface of the modulated porous-layer coating.

size ratio, to simplify the analysis of the transport through the particle stacks making up the modulation.

It is assumed, without visual verification, that there is complete phase separation within the coating so that the vapor escapes from between the stacks and the particle stacks and base layer are completely liquid saturated at all heat fluxes up to the liquid-choking limit. This appears to be reasonable considering that any vapor within the porous matrix of the particle stacks would significantly increase the liquid-drag resistance and likely reduce the q_{CHF} to values well below those measured.

2.2.1 Wetted-Surface Regime

2.2.1.1 Momentum Equation

Based on the preceding assumptions, the liquid is idealized as entering at the top of the stacks, and then flowing down towards the surface. The vapor pressure everywhere in the system is assumed to be constant at the saturation pressure. The flow through the stack is related to the liquid pressure drop and is modeled using the Darcy-Ergun momentum relation [23]

$$0 = -\nabla p_l + \rho_l \mathbf{g} - \frac{\mu_l}{K}\langle \mathbf{u}_l \rangle - \frac{C_E}{K^{1/2}}\rho_l |\langle \mathbf{u}_l \rangle| \langle \mathbf{u}_l \rangle. \tag{2.3}$$

where $\langle \mathbf{u}_l \rangle$ is the volume-averaged liquid velocity vector through the stack. K is the stack permeability, and C_E is the Ergun coefficient. The Carmen-Kozeny model [23] is used for the permeability and results in $K = f(\epsilon)d^2 = \epsilon^3 d^2/[180(1-\epsilon)^2]$ and $C_E = (0.018/\epsilon^3)^{1/2}$. A constant stack porosity of $\epsilon = 0.4$ is assumed for the randomly packed spherical particles.

The particle stack and base layer are divided into regions and zones as shown in Fig. 2.3(c). The liquid is pumped through the stack by capillary and gravity forces

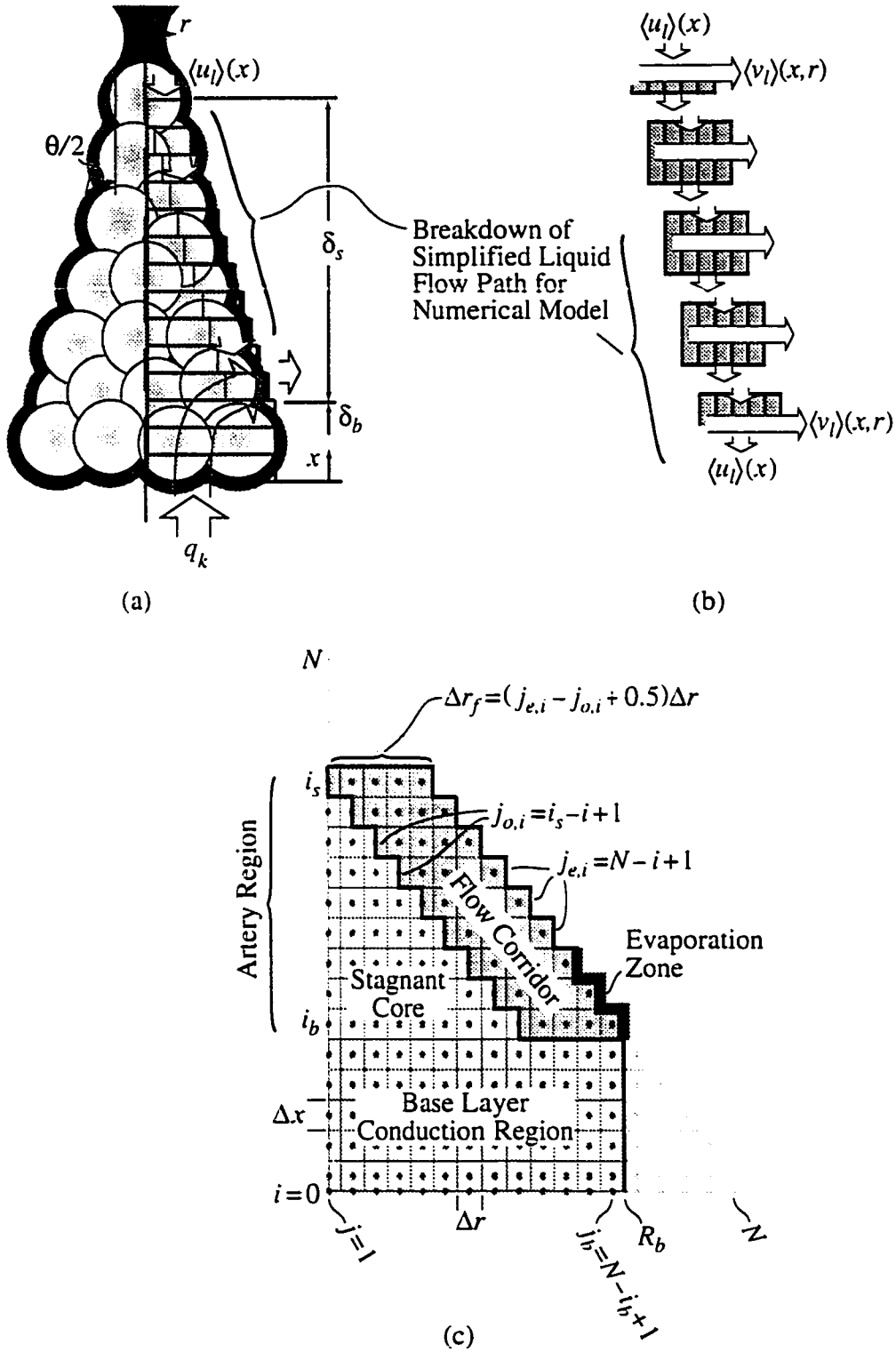

Figure 2.3: Rendering of (a) the heat and liquid flow paths, (b) a schematic showing the breakdown of the liquid flow model used in the calculations, and (c) the various region designations within the particle stack and the discretized computational domain.

to the evaporation zone.

Equation (1.2) enables the determination of the temperature drop from a liquid-vapor interface to the far-field gas saturation temperature as a function of the evaporation heat flux. As an example, a $q_{\mathrm{CHF,max}} = 10^6$ W/m^2 would result in a $\Delta T = 0.28$℃. This is negligible compared to the $T_s - T_{lg}$ across the porous-layer coating, and therefore the added evaporation resistance is not included in the model. The liquid is assumed to undergo thin-film evaporation, with negligible convection thermal resistance, in the evaporation zone around the perimeter of the lower part of the stacks and above the base layer.

The path of least flow resistance between the liquid entrance at the top of the stack and the location of evaporation would be nearer to the outer edge of the stack as opposed to passing through the deep interior. The benefit and likely improvement in accuracy of a fully numerically determined flow field through the stacks under the given assumptions is not large, so an approximate flow channel is assumed along a path of low flow resistance. Therefore, liquid flow is constrained to an annular flow corridor of uniform thickness $\Delta r_f = d/2$ along the side of the stack. Since the flow is assumed to occur only in the stack, the stack contains the fluid artery that feeds the evaporation. Therefore the entire stack is hereafter refered to as the artery region. The remaining interior liquid in the stack core (i.e., not in the flow corridor) and the liquid in the base layer are assumed to be stagnant. The base layer is labeled the conduction region since the heat flux must pass through the base layer by conduction (through the volume-averaged liquid and solid) to reach the evaporation zone.

The conduction and artery regions and the evaporation zone are shown in Fig. 2.3 along with the heat and liquid flow paths and the discretized domain used for the numerical calculations. The discretized, two-dimensional annular flow corridor

in x and r is also shown. For a given row in the artery region, the first node of the flow corridor is denoted as $j_{o,i} = i_s - i + 1$, and the last node (also the outer boundary node of the row) as $j_{e,i} = N - i + 1$. The row at the top of the base layer (at the base height) is labeled i_b, while the row at the center of the topmost particle (at the stack height) is labeled i_s. For flexibility in specifying different geometries, and for ease of computation, the computational domain is a section of an $N \times N$ mesh, where each rectangular unit cell is a cross section of a cylindrical-shell control volume. The computational unit cell facial areas are then determined as

$$A_{x\,1} = \pi(\frac{\Delta r}{2})^2, \quad A_{x\,j=2..N} = 2\pi r_j \Delta r$$
$$A_{r\,j=1..j_{e,i}-1} = 2\pi(r_j + \frac{\Delta r}{2})\Delta x, \quad A_{r\,j_{e,i}} = 2\pi(r_j + \frac{\Delta r}{4})\Delta x. \tag{2.4}$$

The temperature distribution in the particle stack determines the evaporation rate, which is then used to determine the required liquid supply rate (i.e., velocity distribution), as opposed to using the pressure field. The liquid mass flow is assumed to be radially lumped for a given x location. This is shown schematically in Fig. 2.3(b). The liquid velocity (i.e., flow) distribution is then determined from the mass flow distribution by summing the required local evaporation rates along the periphery from $i = i_b \rightarrow i_s$. For a given row i, the radial mass flow is assumed to be constant for all j and equal to that leaving through node $j_{e,i}$ by evaporation. The axial mass flow entering from the row above is then determined as the sum of all the evaporation rates at each row $i_b \rightarrow i$. Since the included cone angle is small, the direction of the mass flow from one row to the next is assumed to be in the x-direction only, and is shifted by $j + 1$ for each descending row to account for the diverging area. The velocities are then adjusted accordingly by multiplying with the

area ratio $A_{x,j}/A_{x,j+1}$.

The simplified flow field is therefore determined by the evaporation rate under the imposed constraints of the localized uniform flow fields as described above, and is determined prior to calculating the pressure drop. The discretized equations determining the liquid velocities in the flow corridor are as follows.

Initializing $j_{e,i} = N - i + 1$ and $j_{o,i} = i_s - i + 1$, then for

$i = i_b \rightarrow i_s$

$$(\dot{M}_l)_{i,j_{e,i}} = \frac{T_{i,j_{e,i}} - T_{lg}}{\Delta h_{lg}(R_{r,ku})_{i,j_{e,i}}}. \qquad (\dot{M}_l)_{\Sigma,i} = [\Sigma_{k=i_b}^{i-1}(\dot{M}_l)_k] + (\dot{M}_l)_{i,j_{e,i}} \qquad (2.5)$$

$$A_{x,f} = \pi[(r_{j_{e,i}} + \frac{\Delta r}{2})^2 - (r_{j_{o,i}} - \frac{\Delta r}{2})^2] \qquad (2.6)$$

$j = j_{o,i} \rightarrow j_{e,i}$

$$\langle (v_l)_{i,j} \rangle = \frac{(\dot{M}_l)_{i,j_{e,i}}}{\rho_l}/A_{r\,j}, \qquad \langle (u_l)_{i,j} \rangle = -\frac{(\dot{M}_l)_{\Sigma,i}}{\rho_l}/A_{x,f}. \qquad (2.7)$$

where

$$(R_{r,ku})_{i,j_{e,i}} = \frac{\Delta r/2}{\langle k \rangle A_{r\,j_{e,i}}} \frac{e^{(\mathrm{Pe}_r)_{i,j_{e,i}}} - 1}{(\mathrm{Pe}_r)_{i,j_{e,i}} e^{(\mathrm{Pe}_r)_{i,j_{e,i}}}}. \qquad (\mathrm{Pe}_r)_{i,j_{e,i}} = \frac{\langle (v_l)_{i,j} \rangle \rho_l c_{p,l} \Delta r}{2\langle k \rangle}.$$

An example of the calculated flow field is shown as a vector plot in Fig. 2.4.

The evaporation along the side of the stack, constituting the evaporation zone, is assumed to alter the local liquid-vapor interface to provide the corresponding interface curvature distribution for the required liquid capillary-pumping through the stack. There is a capillary-limiting minimum radius R_c that corresponds to the capillary pressure of the porous medium, and consequently determines the critical maximum viscous-drag resistance.

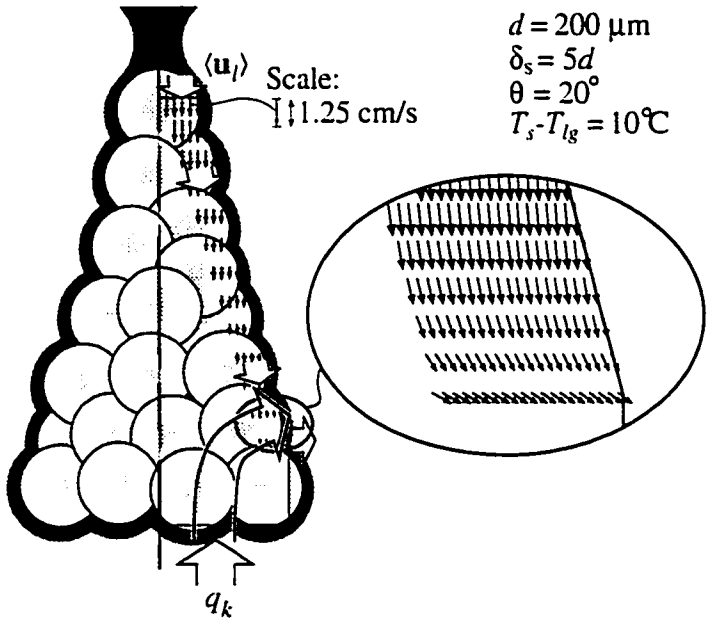

Figure 2.4: A vector plot of the calculated velocity distribution $\langle \mathbf{u}_l \rangle(x)$ in the flow corridor.

Once the flow field is determined, the resulting pressure drop across the stack is calculated and compared with the a maximum available pressure drop (i.e., maximum capillary pumping). If the calculated pressure drop exceeds this maximum pressure drop, then the flow field, and consequently the temperature distribution, is considered impossible. The viscous-drag liquid choking limit is then defined as the heat flux resulting in the evaporation rate (i.e. heat flux) that requires a liquid feed rate corresponding to R_c, or in other words, it is considered to occur when the calculated pressure drop equals this maximum available pressure drop.

Therefore, the maximum sustainable pressure drop across the stack height, δ_s, is assumed to be equal to the capillary pressure $p_c = p_g - p_l = 2\sigma/R_c$ in the porous medium of the stack. From the required velocity distribution, the resulting pressure gradient through the stack as a function of x is found from Eq. (2.3), and is integrated across the artery region from $d \leq x \leq \delta$ to give the total pressure drop.

Ferrel and Alleavitch [45] presented an approximation for the radius of curvature R_c of water saturating a bed of randomly packed spherical particles as $R_c = C_R d/2$, where the ratio of the largest minimum pore diameter to the particle diameter was given as $C_R = 0.41$. Assuming this expression to remain valid for pentane, in a porous medium consisting of spherical particles of $d = 200$ μm, this results in a $p_c = 698$ Pa. The capillary pressure can also be related to a capillary rise height as $p_c = \rho_l g H$. Laboratory tests using these particles with pentane resulted in a $H = 12.7$ cm, which then results in a $p_c = 760$ Pa. This would correspond to $C_R = 0.375$. The Leverett J-function relates the liquid saturation (s), porosity, permeability, and wettability to the capillary pressure through [23]

$$p_g - p_l = p_c = J(s)\frac{\sigma \cos\theta_c Z(\theta_c)}{(K/\epsilon)^{1/2}} = C_J \frac{\sigma}{(K/\epsilon)^{1/2}} \quad \text{for } s = 0, \tag{2.8}$$

where θ_c is the contact angle and is assumed negligible, $Z(\theta_c)$ is the Melrose function and is assumed unity, and $J(s)$ is the Leverett function. The capillary rise height corresponds to the case of a transition from a saturated region to a region of zero saturation (above the rise height). Therefore the maximum capillary pressure corresponds to a constant $C_J = J(s = 0)$. For the data presented by Leverett [23], Schiedeggar [23] determined $C_J = 0.523$, while Udell [23] reported a value of 0.56. Equating $p_c = 4\sigma/(C_R d)$ from Ferrel and Alleavitch [45], with $C_R = 0.375$, to that of Leverett in Eq. (2.8) results in a C_J measured for the particles here of 0.53, in good agreement with the reported values. Therefore, Eq. (2.8) was used with $C_J = 0.53$ to determine the capillary pressure.

From the calculated velocity field, the calculated total pressure drop through the flow corridor is determined by summation of the pressure drop across each row due to an averaged axial velocity in that row, $\langle u_i \rangle_{\Delta r_f}$, which is shown schematically in Fig. 2.3 and determined by

$$\langle u_i \rangle_{\Delta r_f} = \frac{1}{j_{e,i} - j_{o,i} + 1} \sum_{j=j_{o,i}}^{j_{e,i}} u_{i,j}. \tag{2.9}$$

Then following Eq. (2.3), the discretized pressure equations are

$$0 = -\frac{1}{\cos(\theta/2)} \frac{\Delta p_{l,i}}{\Delta x} - \rho g \cos(\theta/2) - \frac{\mu \langle u_i \rangle_{\Delta r_f}}{K \cos(\theta/2)} - \frac{C_E}{K^{1/2} \cos^2(\theta/2)} \rho \langle u_i \rangle_{\Delta r_f} |\langle u_i \rangle_{\Delta r_f}|. \tag{2.10}$$

where the effect of the taper angle is included. The total pressure drop, Δp_Σ, through the flow corridor is then found by

$$\Delta p_{\Sigma} = \sum_{i=i_b}^{i_s} \Delta p_{l,i}. \tag{2.11}$$

The available capillary pumping of the liquid to the evaporation zone is sufficient to sustain the evaporation rate at all heat fluxes up to the viscous-drag liquid-choking limit, where at this limit (i.e., the critical heat flux $q_{\mathrm{CHF,v}}$), the evaporation rate requires a velocity that results in this pressure drop being equal to the capillary pressure, i.e., $\Delta p_{\Sigma} = p_c$.

To determine the evaporation rates, and the resulting flow field and pressure drop across the stack, the temperature distribution must be calculated.

2.2.1.2 Thermal Equilibrium

The liquid and solid phases are assumed to be in local thermal equilibrium (LTE) everywhere within the particle stack since the added complexity of non-local thermal equilibrium (NLTE) is not warranted within the framework of this simplified model. Although the assumption of LTE is not globally valid within the computational domain, it still provides good qualitative results. In the artery region there is a small stagnant core surrounded by an annulus of liquid flowing from the top of the stack to the evaporation zone through the flow corridor. The high velocities in the flow corridor result in a high Peclet number, Pe_{δ}, which acts to resist the flow of heat into the liquid-flow zone and to determine the thickness of the evaporation zone. The high Pe_{δ} indicates that the convection would dominate over the opposing conduction heat transfer processes across the stack height δ, i.e., in the artery region.

The high liquid velocity also results in a large hydrodynamic dispersion term which acts to locally increase the effective thermal diffusion parameter in the flow corridor. Since the heat flux vector is completely consumed by phase change in the small evaporation zone, increases in the local thermal diffusion parameter only

within the flow corridor would have little effect on the resulting q versus $T_s - T_{lg}$ curve. This is because the strong downward convection in the artery region restricts the majority of the heat flux from penetrating too high above the conduction zone (base layer). For $\mathrm{Pe}_d \gg 0.5$, the parallel and perpendicular dispersion coefficients can be expressed as [23],

$$\begin{aligned} \frac{D_{\parallel}^d}{\alpha_l} &= \frac{3}{8}\mathrm{Pe}_d + \frac{1}{12}\pi^2(1-\epsilon)\mathrm{Pe}_d \ln\frac{\mathrm{Pe}_d}{2} \\ \frac{D_{\perp}^d}{\alpha_l} &= \frac{63}{320(2)^{1/2}}(1-\epsilon)^{1/2}\mathrm{Pe}_d, \quad \mathrm{Pe}_d = \frac{(\rho c_p)_l |\langle u_l \rangle| d}{k_l} = \frac{|\langle u_l \rangle| d}{\alpha_l}. \end{aligned} \tag{2.12}$$

For a typical velocity at $q_{\mathrm{CHF,v}}$, $\langle u_l \rangle = 0.1$ m/s. This results in $D_{\parallel}^d/\alpha_l = 745$ and $D_{\perp}^d/\alpha_l = 29$. Since the effective volume-averaged thermal conductivity in the model is assumed isotropic, an isotropic dispersion coefficient was assumed for simplicity to be equal to the larger parallel dispersion coefficient, $D^d = D_{\parallel}^d$, and was included locally in the flow corridor [i.e., in each control volume (i,j) in which $(\langle \mathbf{u}_l \rangle_{i,j})$ was non-zero]. This results in only a slightly larger evaporation zone which in turn results in a negligible shift of the q versus $T_s - T_{lg}$ curve to the left in Fig. 2.1. The difference in the results are assumed to be well within the uncertainty of this simplified model, and therefore further refinement of the inclusion of the dispersion coefficient was considered unnecessary..

From the above discussion, the liquid and solid phases in the artery region (excluding the small evaporation zone) can be assumed always at nearly the pentane saturation temperature, T_{lg}, and to not have large thermal gradients. Therefore, the liquid and solid phases in this region are also assumed to be in LTE.

As an alternative approach to discuss the validity in assuming LTE, the flow through the corridor can be viewed as flow through a single stream heat exchanger,

where the porous matrix consisting of the spheres acts as the bounding surface. Then, an estimation of the number of transfer units (NTU) in the flow corridor can be made. The NTU can be defined as

$$NTU = \frac{A_{ku}\langle \mathrm{Nu}\rangle_d \frac{k_l}{d}}{A_u(\rho c_p)_l \left|\langle u_{l,x}\rangle_{\delta_s}\right|}. \tag{2.13}$$

where A_{ku} is the liquid-solid interfacial area for surface convection and A_u is the flow area, both in the flow corridor, and $|\langle u_{l,x}\rangle_{\delta_s}|$ is the averaged axial velocity through the flow corridor. For a randomly packed system of spherical particles with $d = 200$ μm, an assumed porosity of $\epsilon = 0.4$, a stack height of $\delta = 5d$, and an included cone angle of $\theta = 20°$, the areas would then be $A_{ku} = 1.56 \times 10^{-6}$ m^2, and $A_u = 8.68 \times 10^{-8}$ m^2. The fluid properties are listed in Table 3.1. To determine the $\langle \mathrm{Nu}\rangle_d$, an empirical expression was used for surface convection through a packed bed of particles and is given as [46]

$$\langle \mathrm{Nu}\rangle_d = 2 + (0.4\mathrm{Re}_d^{1/2} + 0.2\mathrm{Re}_d^{2/3})\mathrm{Pr}^{0.4}, \quad \text{where} \quad \mathrm{Re}_d = \frac{\rho_l \left|\langle u_{l,x}\rangle_{\delta_s}\right| d}{\mu_l(1-\epsilon)}. \tag{2.14}$$

For an average velocity of $|\langle u_{l,x}\rangle_{\delta_s}| = 0.1$ m/s (typical order of magnitude of the numerical results near the predicted $q_{\mathrm{CHF,v}}$ this geometry), the $\langle \mathrm{Nu}\rangle_d = 17.2$. Then the $NTU = 1.2$. This would indicate that the heat exchanger effectiveness of the flow corridor is around 0.6 at this theoretical operating condition and that LTE would not be a valid assumption. Evaluating the NTU at more realistic operating conditions of $|\langle u_{l,x}\rangle_{\delta_s}| = 0.0125$ m/s (determined from the numerical model for $T_s - T_{lg} = 10$℃), the $\langle \mathrm{Nu}\rangle_d = 6.6$ resulting in an $NTU = 3.5$. This would indicate that the heat exchanger effectiveness of the flow corridor is near unity and LTE would be a valid assumption. As the heat flux (and correspondingly the $T_s - T_{lg}$) decreases, the average

liquid velocity decreases resulting in a longer residence time of the liquid in the flow corridor allowing the liquid and solid phases to reach LTE. This would indicate that the assumption of LTE becomes more valid the further the system operates in the wetted-surface regime away from the q_{CHF} point. This analysis does not include the effect of the evaporation at the end of the flow corridor consuming the incoming heat flux. Since the evaporation zone consumes most of the heat flux, and since the high Pe would indicate a high convection effect working to restrict the heat from penetrating too far up into the artery region, the temperatures in the majority of the artery region are expected to be nearly equal to T_{lg}, and therefore this region is still assumed to be in LTE for simplification purposes. Figure 2.5 shows the variation of NTU versus particle diameter for constant δ_s/d, $|\langle u_{l,x}\rangle_{\delta_s}|$, and fluid properties. From this plot it can be seen that the assumption of LTE becomes increasingly valid with decreasing d.

In the conduction zone, the liquid is assumed to be stagnant, and at steady state conditions and neglecting thermobuoyant motion, the liquid and solid phases here can be assumed to be in LTE as well. The assumption of LTE within the evaporation zone is least valid, but since this zone constitutes such a small part of the domain, the invalidity of the assumption negligibly affects the predictions.

2.2.1.3 Energy Equation

Assuming LTE, the temperature distribution is modeled following

$$\nabla \cdot [(\rho c_p)_l \langle \mathbf{u}_l \rangle \langle T \rangle - (\langle k \rangle + \langle k \rangle^d) \nabla \langle T \rangle] = \begin{cases} 0 & r_j < r_{j_{e,i}} \\ \nabla \cdot (\rho_l \langle \mathbf{u}_l \rangle \Delta h_{lg}) & r_j = r_{j_{e,i}}, \end{cases} \tag{2.15}$$

which can be nondimensionalized and scaled with δ as

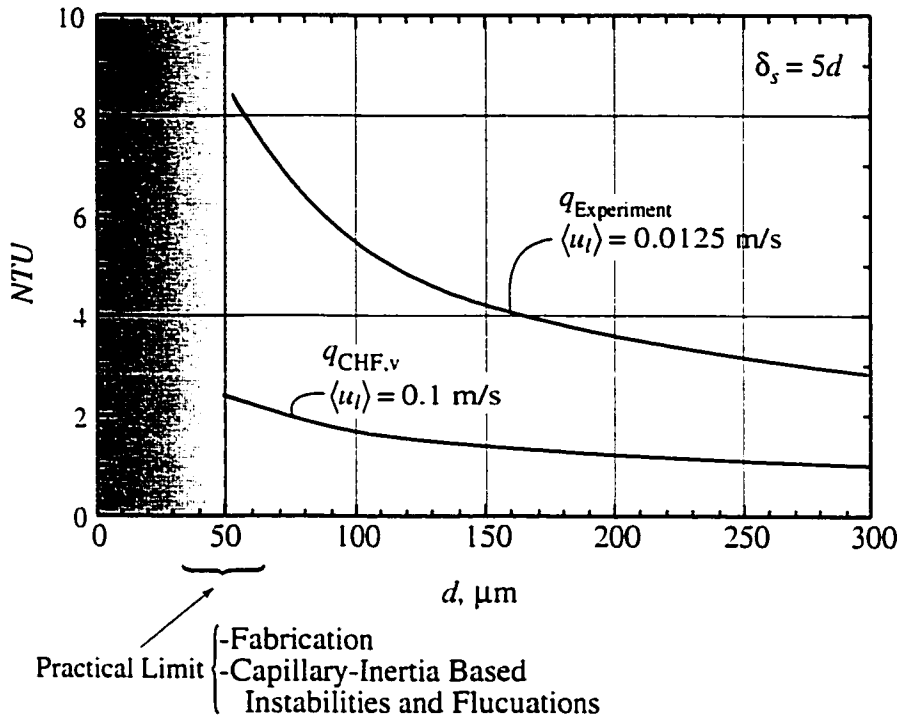

Figure 2.5: The variation in the NTU with respect to particle diameter d for $\delta_s = 5d$.

$$\nabla \cdot [\mathrm{Pe}_\delta \mathbf{u}_l^* T^* + (1 + \frac{\langle k \rangle^d}{\langle k \rangle}) \nabla T^*] = \begin{cases} 0 & r_j < r_{j_{e,i}} \\ \nabla \cdot \mathrm{Pe}_\delta \mathbf{u}_l^* / \mathrm{Ja} & r_j = r_{j_{e,i}}, \end{cases} \tag{2.16}$$

where

$$\mathrm{Pe}_\delta = \frac{(\rho c_p)_l \, \delta \, |\langle u_l \rangle|_{\theta=0}}{\langle k \rangle}, \quad \mathrm{Ja} = \frac{c_{p,l}(T_s - T_{lg})}{\Delta h_{lg}}, \quad T^* = \frac{\langle T \rangle - T_{lg}}{T_s - T_{lg}}, \quad \mathbf{u}_l^* = \frac{\langle \mathbf{u}_l \rangle}{|\langle u_l \rangle|_{\theta=0}}$$

and where $\langle T \rangle$ is the local volume-averaged temperature, $\langle k \rangle$ is the volume-averaged effective stagnant thermal conductivity, $\langle k \rangle^d = (\rho c_p)_l D^d$ is the dispersion contribution to the total thermal conductivity ($\langle k \rangle + \langle k \rangle^d$), $|\langle u_l \rangle|_{\theta=0}$ is a constant for a given q and is the maximum velocity corresponding to a cylindrical stack, and the evaporation term (right hand side of the equation) is assumed zero everywhere except on the side boundaries of the stack.

The volume-averaged stagnant thermal conductivity is assumed constant and is predicted by the modified Zehner-Schlunder model [47] accounting for a sintered contact area and an assumed porosity. In this model, $\langle k \rangle$ is related to a particle shape factor, B, a particle deformation factor, a, and the liquid and solid thermal conductivities, k_l and k_s, as

$$\frac{\langle k \rangle}{k_l} = (1 - F_1) - \frac{F_1}{k_l/k_s}(1 - \frac{1}{F_2^2}) + \frac{2F_1}{F_2 - F_3} \left[\frac{(B-1) + F_2 - F_3}{(F_2 - F_3)^2} \ln \frac{F_2}{F_3} - \right.$$

$$\left. \frac{(B-1) + 2F_2}{2F_2^2} - \frac{B-1}{F_2(F_2 - F_3)} \right], \tag{2.17}$$

where

$$F_1 = (1-\epsilon)^{1/2}, \qquad F_2 = 1 + aB, \qquad F_3 = (1+a)B\, k_l/k_s.$$

The contact diameter, d_c is related to B and a by

$$\frac{d_c}{d} = 1 - \frac{1}{(1+aB)^2}, \tag{2.18}$$

and ϵ is related to B and a by

$$\epsilon = 1 - \frac{B^2}{(B-1)^6 F_2^2}\left\{ [(B-1)^2 - 2(B-1)] + \right.$$

$$\left. 2(1+a)F_2 \ln\frac{F_3}{F_2 k_l/k_s} + a(B-1)[(B-1)^2 - 2] \right\}^2. \tag{2.19}$$

For a $d_c = 0.15d$, and an $\epsilon = 0.4$, Eqs. (2.18) and (2.19) can be solved simultaneously to find $B = 1.97$ and $a = 5.82 \times 10^{-3}$ for a pentane/copper system. Using these factors in Eq. (2.17), the effective stagnant thermal conductivity is found to be $\langle k \rangle = 9$ W/m^2-K .

The upwards heat flux is in part resisted by the downwards convection due to the liquid flow in the stack within the annular flow corridor. The heat flux is drawn towards the liquid-vapor interface along the periphery near the bottom of the stack (i.e. the evaporation zone starting at the top of the base layer at $x = d$) to provide the heat for evaporation (i.e., the liquid-vapor phase change). The heat flux is then conserved as it is conducted through the base layer, and then the magnitude of the heat flux conducting upwards through the stack (i.e., artery region) diminishes to zero at some height as it is completely consumed. Currently, the model predicts this height to be less than one particle diameter from the base of the stack.

The temperature distribution must be calculated to determine the evaporation rates, and the resulting flow field and required pressure drop, in order to predict the $q_{\mathrm{CHF,v}}$. The temperature distribution is determined using the discretized finite-volume form of Eq. (2.15). The boundary conditions for the system are an evaporation heat flux to a constant vapor temperature $T_g = T_{lg}$ on the side of the stacks [$r(x)$ from $i_b < i < i_s$], an insulated vertical side through the symmetry plane in the base layer [$r(x) = R_b$ from $0 < i < i_b - 1$], a constant saturation temperature on the top ($j, i = i_s$), and a constant input heat flux at the bottom surface ($j, i = 0$). The temperature distribution is therefore predicted as a function of the input surface heat flux. The surface superheat is then determined for each prescribed flux as the area-averaged predicted base temperature $T_s - T_{lg} = \langle T \rangle|_{x=0}$. The discretized energy equations are as follows, where $T = \langle T \rangle = \langle T \rangle^s = \langle T \rangle^l$.

Conduction zone:

Boundary on bottom surface:

$$\frac{T_s - T_{i+1,j}}{(R_{x,k})_{0,j}} = q(A_x)_j \qquad i = 0, j = 1 \rightarrow N - i_b + 1. \tag{2.20}$$

Base layer nodes:

For $i = 1 \rightarrow i_b - 1$:

$$\frac{T_{i,j} - T_{i-1,j}}{(R_{x,k})_{i-1,j}} + \frac{T_{i,j} - T_{i+1,j}}{(R_{x,k})_{i,j}} + \frac{T_{i,j} - T_{i,j-1}}{(R_{r,k})_{i,j-1}} + \frac{T_{i,j} - T_{i,j+1}}{(R_{r,k})_{i,j}} = 0$$
$$j = 2 \rightarrow N - i_b. \tag{2.21}$$

$$\frac{T_{i,j}-T_{i-1,j}}{(R_{x,k})_{i-1,j}}+\frac{T_{i,j}-T_{i+1,j}}{(R_{x,k})_{i,j}}+\frac{T_{i,j}-T_{i,j-1}}{(R_{r,k})_{i,j-1}}=0 \qquad j=N-i_b+1, \tag{2.22}$$

Artery region:

Initializing $j_{e,i}=N-i+1$ and $j_{o,i}=i_s-i+1$, then

For $i=i_b$:

$$\frac{T_{i,j}-T_{i-1,j}}{(R_{x,k})_{i-1,j}}+\frac{T_{i,j}-T_{i+1,j}}{(R_{x,k})_{i,j}}+\frac{T_{i,j}-T_{i,j-1}}{(R_{r,k})_{i,j-1}}+\frac{T_{i,j}-T_{i,j+1}}{(R_{r,k})_{i,j}}=0$$

$$j=2\rightarrow j_{o,i}-1. \tag{2.23}$$

$$\frac{T_{i,j}-T_{i-1,j}}{(R_{x,k})_{i-1,j}}+\frac{T_{i,j}-T_{i+1,j}}{(R_{x,ku})_{i,j}}+\frac{T_{i,j}-T_{i,j-1}}{(R_{r,k})_{i,j-1}}+\frac{T_{i,j}-T_{i,j+1}}{(R_{r,ku})_{i,j}}=0 \qquad j=j_{o,i}. \tag{2.24}$$

$$\frac{T_{i,j}-T_{i-1,j}}{(R_{x,k})_{i-1,j}}+\frac{T_{i,j}-T_{i+1,j}}{(R_{x,ku})_{i,j}}+\frac{T_{i,j}-T_{i,j-1}}{(R_{r,ku})_{i,j-1}}+\frac{T_{i,j}-T_{i,j+1}}{(R_{r,ku})_{i,j}}=0.$$

$$j=j_{o,i}+1\rightarrow j_{e,i}-1. \tag{2.25}$$

$$\frac{T_{i,j}-T_{i-1,j}}{(R_{x,k})_{i-1,j}}+\frac{T_{i,j}-T_{i,j-1}}{(R_{r,ku})_{i,j-1}}+\frac{T_{i,j}-T_{lg}}{(R_{r,ku})_{i,j_{e,i}}}=0 \qquad j=j_{e,i}. \tag{2.26}$$

For $i=i_b+1\rightarrow i_s-1$:

$$\frac{T_{i,j}-T_{i-1,j}}{(R_{x,k})_{i-1,j}}+\frac{T_{i,j}-T_{i+1,j}}{(R_{x,k})_{i,j}}+\frac{T_{i,j}-T_{i,j-1}}{(R_{r,k})_{i,j-1}}+\frac{T_{i,j}-T_{i,j+1}}{(R_{r,k})_{i,j}}=0$$

$$j=2\rightarrow j_{o,i}-1, \tag{2.27}$$

$$\frac{T_{i,j}-T_{i-1,j}}{(R_{x,k})_{i-1,j}}+\frac{T_{i,j}-T_{i+1,j}}{(R_{x,ku})_{i,j}}+\frac{T_{i,j}-T_{i,j-1}}{(R_{r,k})_{i,j-1}}+\frac{T_{i,j}-T_{i,j+1}}{(R_{r,ku})_{i,j}}=0$$

$$j=j_{o,i}, \quad (2.28)$$

$$\frac{T_{i,j}-T_{i-1,j}}{(R_{x,ku})_{i-1,j}}+\frac{T_{i,j}-T_{i+1,j}}{(R_{x,ku})_{i,j}}+\frac{T_{i,j}-T_{i,j-1}}{(R_{r,ku})_{i,j-1}}+\frac{T_{i,j}-T_{i,j+1}}{(R_{r,ku})_{i,j}}=0,$$

$$j=j_{o,i}+1 \rightarrow j_{e,i}-1, \quad (2.29)$$

$$\frac{T_{i,j}-T_{i-1,j}}{(R_{x,ku})_{i-1,j}}+\frac{T_{i,j}-T_{i,j-1}}{(R_{r,ku})_{i,j-1}}+\frac{T_{i,j}-T_{lg}}{(R_{r,ku})_{i,j_{e,i}}}=0 \qquad j=j_{e,i}, \quad (2.30)$$

For $i=i_s$:

$$\frac{T_{i,j}-T_{i-1,j}}{(R_{x,k})_{i-1,j}}+\frac{T_{i,j}-T_{i,j+1}}{(R_{r,ku})_{i,j}}=0 \qquad j=j_{o,i}, \quad (2.31)$$

$$\frac{T_{i,j}-T_{i-1,j}}{(R_{x,ku})_{i-1,j}}+\frac{T_{i,j}-T_{i,j-1}}{(R_{r,ku})_{i,j-1}}+\frac{T_{i,j}-T_{i,j+1}}{(R_{r,ku})_{i,j}}=0 \qquad j=j_{o,i}+1 \rightarrow j_{e,i}-1, \quad (2.32)$$

$$\frac{T_{i,j}-T_{i-1,j}}{(R_{x,ku})_{i-1,j}}+\frac{T_{i,j}-T_{i,j-1}}{(R_{r,ku})_{i,j-1}}+\frac{T_{i,j}-T_{lg}}{(R_{r,ku})_{i,j_{e,i}}}=0 \qquad j=j_{e,i}, \quad (2.33)$$

Center column of nodes:

$$\frac{T_{i,1} - T_{i+1,1}}{(R_{x,k})_{i,1}} + \frac{T_{i,1} - T_{i,2}}{(R_{r,k})_{i,1}} = 0 \qquad j = 1, i = 1 \rightarrow i_s - 1, \tag{2.34}$$

where

$$(R_{x,k})_{i,j} = \frac{\Delta x}{\langle k \rangle A_{x\,j}}, \qquad (R_{x,k})_{0,j} = \frac{\Delta x/2}{\langle k \rangle A_{x\,j}}. \tag{2.35}$$

$$(R_{x,ku})_{i,j} = \frac{\Delta x}{(\langle k \rangle + \langle k \rangle^d) A_{x\,j}} \frac{e^{(\mathrm{Pe}_x)_{i,j}} - 1}{(\mathrm{Pe}_x)_{i,j}\, e^{(\mathrm{Pe}_x)_{i,j}}}. \tag{2.36}$$

$$(R_{r,k})_{i,j} = \frac{\ln(r_{j+1}/r_j)}{2\pi \langle k \rangle \Delta x}, \quad (R_{r,k})_{i,j-1} = \frac{\ln(r_j/r_{j-1})}{2\pi \langle k \rangle \Delta x}, \quad (R_{r,k})_{i,1} = \frac{\Delta r}{\langle k \rangle A_{r\,1}}. \tag{2.37}$$

$$(R_{r,ku})_{i,j} = \frac{\Delta r}{(\langle k \rangle + \langle k \rangle^d) A_{r\,j}} \frac{e^{(\mathrm{Pe}_r)_{i,j}} - 1}{(\mathrm{Pe}_r)_{i,j}\, e^{(\mathrm{Pe}_r)_{i,j}}}. \tag{2.38}$$

and

$$(\mathrm{Pe}_x)_{i,j} = \frac{\langle (u_l)_{i,j} \rangle \rho_l c_{p,l} \Delta x}{\langle k \rangle}, \qquad (\mathrm{Pe}_r)_{i,j} = \frac{\langle (v_l)_{i,j} \rangle \rho_l c_{p,l} \Delta r}{\langle k \rangle}. \tag{2.39}$$

2.2.1.4 Slope of Wetted-Surface Regime

At all heat fluxes below that resulting in the viscous-drag choking limit, there exists sufficient liquid pumping through the flow corridor to the evaporation zone to feed the liquid-vapor phase change. Since the resistance for evaporation is assumed negligible, all of the available heat flux is used for liquid-vapor phase change within a short evaporation zone, on the order of less than $0.5d$, above which the volume-averaged temperatures would be equal to the saturation temperature T_{lg}. Below the evaporation zone, in the base layer, the heat flux is assumed to be by conduction only. Calculations show that the heat flux through the base layer is indeed nearly one-dimensional in the x-direction, before converging towards the evaporation zone at the top of the base layer. This can be seen from the example plot of the calculated temperature profiles shown in Fig. 2.6, one for $T_s - T_{lg} = 10$℃ corresponding to the typical magnitude of the measurements, and another for $T_s - T_{lg} = 149$℃ corresponding to the predicted (i.e. theoretical) $q_{\mathrm{CHF,v}}$. Therefore, assuming a linear temperature profile from the surface to the evaporation zone, to approximate a one-dimensional heat flux, a characteristic length, $L_k = C_k d$, would exist that would account for the effect of the cylindrical geometry, the turning of the heat flux towards the evaporation zone (peripheral surface), plus an additional average effective height above the top of the base layer and into the evaporation zone. The heat flux in the wetted-surface regime can then be approximately related to the surface superheat, $T_s - T_{lg}$, by

$$q = -\langle k \rangle \nabla T = \langle k \rangle \frac{T_s - T_{lg}}{C_k d}. \tag{2.40}$$

Since the geometry is scaled with d, C_k is independent of particle size for a given

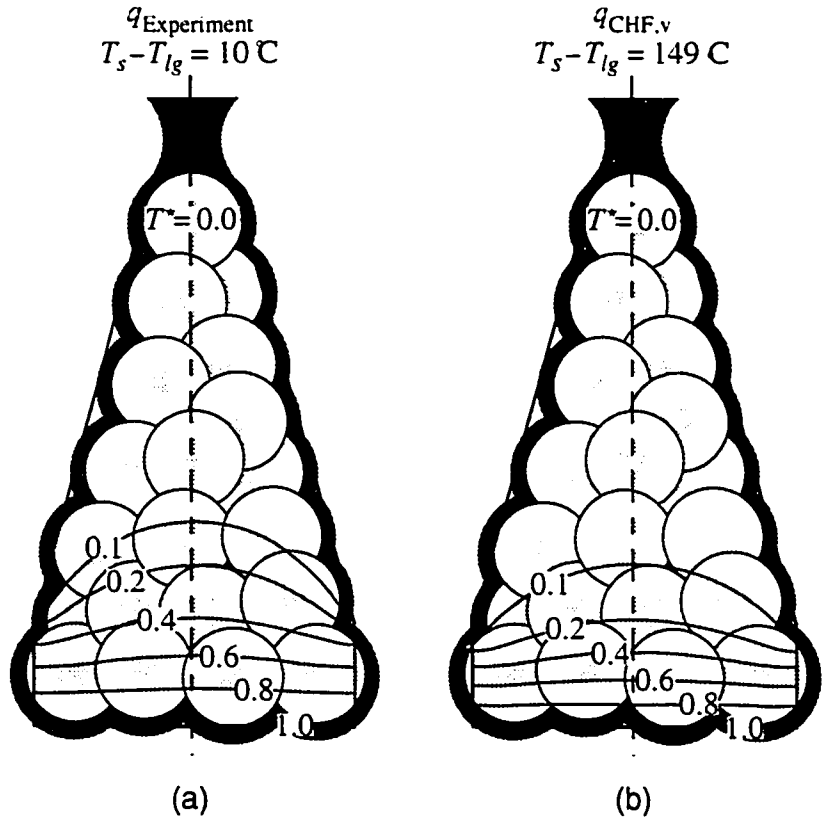

Figure 2.6: A contour plot of the predicted temperature distribution within the base layer and the particle stack for (a) $T_s - T_{lg} = 10$℃ corresponding to the typical magnitude of the measurements, and (b) $T_s - T_{lg} = 149$℃ corresponding to the predicted (i.e. theoretical) $q_{CHF,v}$.

geometry. For a conical stack geometry, C_k is dominantly dependent on the height of the base layer $\delta_b = C_b d$, and the base diameter of the stack. The base diameter is characterized by the stack height, $\delta_s = C_\delta d$, and the included angle of the cone, θ. Therefore, the functional dependence of the conduction coefficient is approximated as $C_k = f(C_\delta, \theta, C_b)$. For a base layer of height $\delta_b = C_b d = 1d$, the constant C_k would be expected to be slightly greater than unity (i.e., L_k is expected to be slightly greater than δ_b, or in other words, C_k is expected to be slightly greater than C_b). Numerically solving for q as a function of $T_s - T_{lg}$, a constant value of $C_k = 1.22$ was found for this conical stack geometry characterized by $\theta = 20°$, $C_\delta = 4$, and $C_b = 1$.

From Eq. (2.40), the q versus $T_s - T_{lg}$ curve in the wetted-surface regime prior to the critical heat flux can be predicted.

2.2.2 Viscous-Drag Liquid-Choking Limit

As mentioned, the evaporation along the side of the stack requires a certain rate of liquid supply which determines the liquid velocity distribution $\langle \mathbf{u}_l \rangle(x)$. As the evaporation (i.e., heat flux) is increased, the liquid flow must increase. This results in an increased viscous-drag resistance within the particle stack. The viscous-drag liquid-choking limit is then determined by a balance between the rate of liquid evaporation and the ability for the liquid to be resupplied through the stack. These flow paths were shown in Fig. 2.2.

Recall that the liquid is assumed to be pumped through the artery region by capillary and gravity forces. The relative importance of the gravity forces to the capillarity is described by the Bond number given as

$$\mathrm{Bo}_d = \frac{g\rho_l d^2}{\sigma}. \tag{2.41}$$

For pentane liquid and with $d = 200$ μm, this results in $\mathrm{Bo}_d = 0.02$, thus indicating that gravity is negligible within the stack, but it is still included in model to allow for variation of d.

The evaporation along the side of the stack is assumed to alter the local liquid-vapor interfaces to provide the required interface curvature distribution for the liquid capillary-pumping through the stack. There then exists a capillary-limiting minimum radius R_c that corresponds to the capillary pressure for the porous media, and consequently determines the critical-maximum viscous-drag resistance. The viscous-drag liquid choking limit is then defined as the heat flux resulting in the evaporation rate (i.e. heat flux) that requires a liquid feed rate corresponding to $-dp/dx = p_c/\delta_s$.

The viscous-drag liquid-choking limit (i.e., the critical heat flux $q_{\mathrm{CHF},v}$) is then considered to be at the flux requiring a velocity that results in this pressure drop being equal to the capillary pressure, i.e., $\Delta p_\Sigma = p_c$.

An analytical approximation for the $q_{\mathrm{CHF},v}$ can be found by making a few further simplifications. Assuming that the effect of variable flow area (i.e., assuming cylindrical instead of conical stacks, $\theta \to 0$) is negligible, and that all of the liquid flows the full length δ_s through the flow corridor before evaporating, then the pressure gradient through the vertical flow corridor would be linear. Further, assuming that the effect of gravity is negligible (i.e., Bo_d is small), a characteristic length scale is $K^{1/2}$, and noting $u(x) < 0$, then Eq. (2.10) can be simplified for a one-dimensional system to be

$$0 = -\frac{dp^*}{dx^*} + \mathrm{Ca} + \mathrm{We}_{K^{1/2}} \qquad (\theta = 0) \tag{2.42}$$

where dp^*/dx^* is a dimensionless and normalized pressure gradient, and where We

is the Weber number, Ca is the Capillary number, each defined as

$$\mathrm{We}_{K^{1/2}} = \frac{\rho_l \langle u_l \rangle^2 K^{1/2}}{\sigma} \frac{C_{\mathrm{E}} \delta_s}{C_J (K\epsilon)^{1/2}}, \qquad \mathrm{Ca} = \frac{|\langle u_l \rangle| \mu_l}{\sigma} \frac{\delta_s}{C_J (K\epsilon)^{1/2}}, \qquad C_j = 0.53.$$

In Eq. (2.42), the solution would indicate the maximum velocity achievable by the available capillary pumping power. This velocity would not be that experienced within the experimental stack, but rather represents an upper limit that is dependent on the permeability and stack height, $K(d)$ and $\delta_s(d)$, and therefore on the particle size, d. The velocity in the stack can then be classified as a fraction of this maximum velocity [corresponding to a maximum viscous-drag liquid-choking limit, $(q_{\mathrm{CHF,v}})_{\theta=0}$], where the ratio would depend on the stack geometric parameters such as the included cone angle.

The velocity, $\langle u_l \rangle$, can be written in terms of the critical heat flux and an area fraction, ϵ_s, defined as the ratio of the cone-base area to the unit-cell surface area, as

$$\langle u_l \rangle = \frac{(q_{\mathrm{CHF,v}})_{\theta=0}}{\epsilon_s \rho_l \Delta h_{lg}}. \tag{2.43}$$

Recursively solving Eq. (2.42) for u through the flow corridor, and substituting Eq. (2.43) for u, an expression for the maximum viscous-drag liquid-choking limit, $(q_{\mathrm{CHF,v}})_{\theta=0}$, can be found as

$$\frac{(q_{\mathrm{CHF,v}})_{\theta=0}}{\epsilon_s C_J \dfrac{\rho_l \sigma \Delta h_{lg}}{\mu_l} \dfrac{(K\epsilon)^{1/2}}{\delta_s}} = 1 - \frac{C_{\mathrm{E}}}{C_J} \frac{\delta_s}{\epsilon_s^2 \epsilon^{1/2}} \frac{(q_{\mathrm{CHF,v}})_{\theta=0}^2}{\rho_l \sigma \Delta h_{lg}^2}. \tag{2.44}$$

In this recursive form, the effect of particle diameter on the $(q_{\mathrm{CHF,v}})_{\theta=0}$ can be seen. Since the stack height, δ_s, and the square root of permeability, $K^{1/2}$ are assumed

each directly proportional to d, the effect of d is consolidated into the second term of the right hand side of Eq. (2.44). As $d \to 0$, then the right hand side of Eq. (2.44) equals unity. Equation (2.44) was scaled with the solution to the viscous limit of Eq. (2.42), namely the solution to $\mathrm{Ca} = dp^*/dx^*$. Therefore, as d decreases, viscous forces dominate over inertial forces, and in the limit, a maximum $q_{\mathrm{CHF,v}}$ exists as

$$(q_{\mathrm{CHF,v}})_{\theta=0} = \epsilon_s C_J \frac{\rho_l \sigma \Delta h_{lg}}{\mu_l} \frac{(K\epsilon)^{1/2}}{\delta_s} = \frac{\mathrm{We}_{K^{1/2}}}{\mathrm{Ca}^2} \frac{\mu_l \Delta h_{lg}}{C_{\mathrm{E}} K^{1/2}} \qquad d \to 0, \tag{2.45}$$

or

$$\frac{(q_{\mathrm{CHF,v}})_{\theta=0}}{\epsilon_s C_J \dfrac{\rho_l \sigma \Delta h_{lg}}{\mu_l} \dfrac{(K\epsilon)^{1/2}}{\delta_s}} = 1 \qquad d \to 0. \tag{2.46}$$

Equation (2.43) can be used with Eq. (2.42) to also explicitly solved for $(q_{\mathrm{CHF,v}})_{\theta=0}$ as

$$\frac{(q_{\mathrm{CHF,v}})_{\theta=0}}{\dfrac{\mathrm{We}_{K^{1/2}}}{\mathrm{Ca}^2} \dfrac{\mu_l \Delta h_{lg}}{C_{\mathrm{E}} K^{1/2}}} = -\frac{1}{2\dfrac{\mathrm{We}_{K^{1/2}}}{\mathrm{Ca}^2}} + \left[\left(\frac{1}{2\dfrac{\mathrm{We}_{K^{1/2}}}{\mathrm{Ca}^2}}\right)^2 + \frac{1}{\dfrac{\mathrm{We}_{K^{1/2}}}{\mathrm{Ca}^2}}\right]^{1/2}. \tag{2.47}$$

The cone-base area to unit-cell surface area ratio, ϵ_s, is included to account for the different patterns of the stack modulations across the surface. For example, for adjacent single-height stacks in a square array, $\epsilon_s = \pi/4 = 0.785$, and for an hexagonal array, $\epsilon_s = 3^{1/2}\pi/6 = 0.907$.

For cases when $\theta > 0$, a coefficient $0 < C_\theta(\theta) \leq 1$ can be used to adjust the maximum velocity found in Eq. (2.42) to account for the effect of variable flow area (i.e., conical sidewalls as opposed to a cylindrical stack), as computed with the numerical model. Therefore, the unit-cell critical heat flux (i.e., surface viscous-drag

liquid-choking limit), corresponding to the $q_{CHF,v}$ calculated from the model, can be approximated as

$$q_{CHF,v} = C_\theta (q_{CHF,v})_{\theta=0}, \tag{2.48}$$

or

$$\frac{q_{CHF,v}}{C_\theta \epsilon_s C_J \dfrac{\rho_l \sigma \Delta h_{lg}}{\mu_l} \dfrac{(K\epsilon)^{1/2}}{\delta_s}} = 1 - \frac{C_E}{C_J C_\theta^2} \frac{\delta_s}{\epsilon_s^2 \epsilon^{1/2}} \frac{q_{CHF,v}^2}{\rho_l \sigma \Delta h_{lg}^2}. \tag{2.49}$$

where C_θ is an empirical function of θ found by taking the ratio as a function of θ of the numerical results and that predicted by Eq. (2.47). The function C_θ was found to be negligible dependent on d within the range of interest 50 μm $\leq d \leq$ 200 μm. The variation of C_θ versus θ is shown in Fig. 2.7.

The viscous-drag liquid-choking model presents a means of determining the q versus $T_s - T_{lg}$ relationship and the $q_{CHF,v}$ corresponding to the theoretical viscous-drag liquid-choking limit within the stack. It is highly dependent on the model used for treating the porous medium as well as the assumed simplified liquid-flow paths, but as a first approach, it appears to have qualitative agreement with the experimental results to be presented.

2.2.3 Hydrodynamic Liquid-Choking Limit

A hydrodynamically determined liquid-choking limit $q_{CHF,h}$ has been proposed in addition to $q_{CHF,v}$. The modulated porous-layer coating can create designed (non-hydrodynamically determined) locations of vapor escape into the liquid pool altering the thermal-hydraulics in the pool and above the layer, thus extending the classical

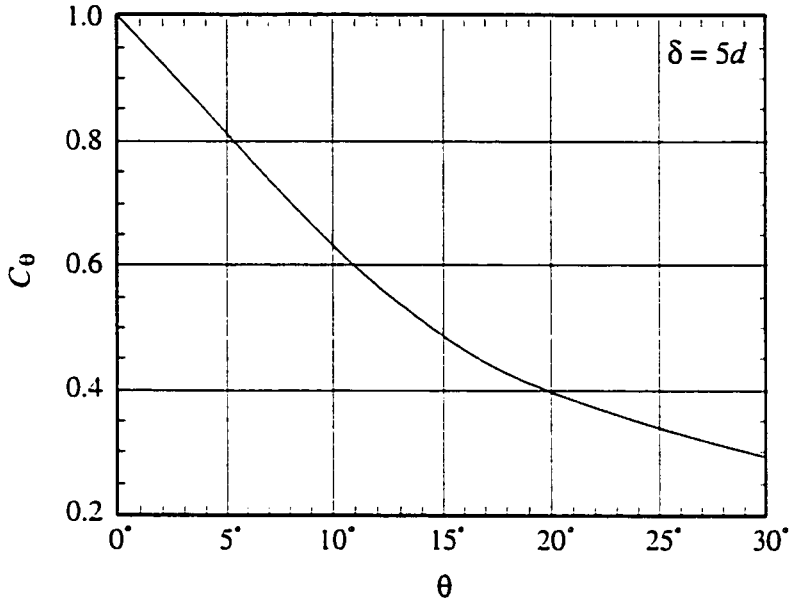

Figure 2.7: The calculated variation of the coefficient C_θ as a function of included angle of a conical stack (for 50 μm $\leq d \leq$ 300μm).

hydrodynamic liquid-choking limit. This model, therefore, considers the ability for the liquid to flow towards the surface through the escaping vapor.

Zuber [25] developed a mechanistic theoretical model for the q_{CHF} based on idealized hydrodynamics of a liquid-vapor interface system above the surface. Idealizing the vapor flow, he equated the boiling heat transfer Q to the rate of heat escape by buoyant flow of the vapor through the liquid as

$$Q = \rho_g u_g h_{fg} A_g, \tag{2.50}$$

where A_g is the cross-sectional flow area for vapor escape above a representative (spatial periodicity assumed) portion of the surface. Then the maximum heat transfer Q_{CHF} was when the vapor enthalpy approached the latent heat resulting in an expression for q_{CHF} as

$$q_{\mathrm{CHF}} = \frac{Q_{\mathrm{CHF}}}{A_b} = \rho_g u_g \Delta h_{lg} \frac{A_g}{A_b}. \tag{2.51}$$

where A_b is the base surface area of a representative cell beneath A_g, i.e. $A_b = A_g + A_l$. Figure 2.8 repeats part of Fig. 1.6 for convenience and shows a rendering of the determination of A_g and A_b. Zuber hypothesized that the base surface area A_b corresponds to a periodic cell determined by a flow-critical, base length scale λ_b of the fluid, i.e., $A_b = \lambda_b^2$. From the spacings determined by λ_b, the vapor bubbles would then flow from the surface (i.e., break through the liquid) through idealized cylindrical vapor-flow channels of area $A_g = \pi R_g^2$, where radius $R_g = a\lambda_b$, and where a is the to be determined ratio of R_g/λ_b. In this model, as the heat flux is increased, the vapor velocity increases until the liquid-vapor interface of the channel

Perspective View

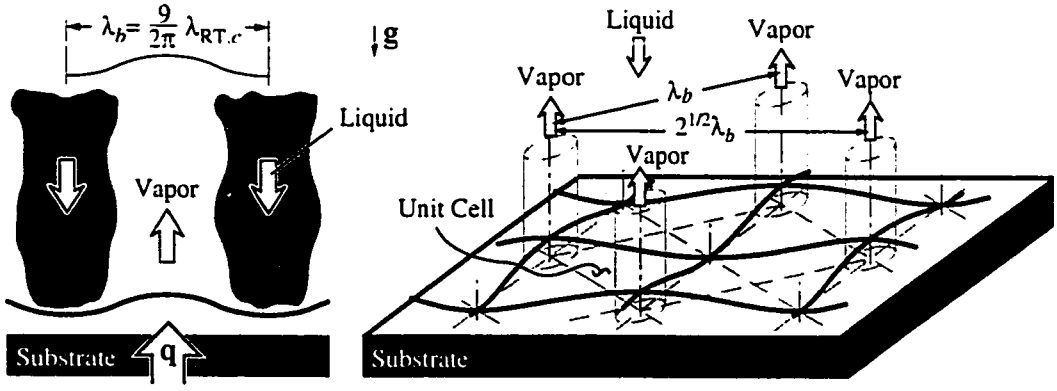

Top View

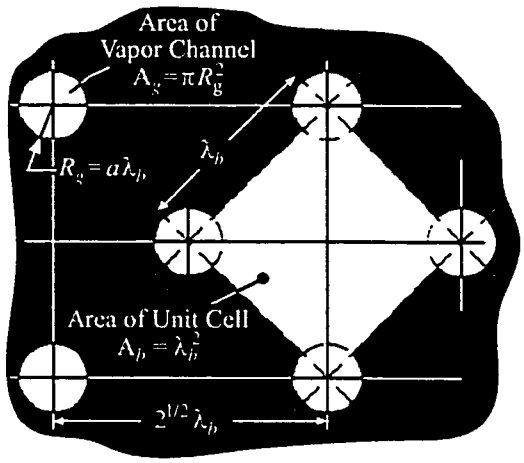

Figure 2.8: Rendering of the geometry for the liquid-vapor counter flow hydrodynamics. (Redrawn based on figures by Lienhard and Witte [30])

walls becomes unstable. For a vapor flowing adjacent to a liquid with the liquid-vapor interface parallel to gravity, the critical-flow length scale along the interface as a function of vapor velocity corresponds to the Kelvin-Helmholtz instability wavelength as [25]

$$\lambda_{KH} = \frac{2\pi\sigma}{\rho_g u_g^2} \quad \text{or} \quad u_g = \left(\frac{2\pi\sigma}{\lambda_{KH}\rho_g}\right)^{1/2}. \tag{2.52}$$

Substituting Eq. (2.52) into Eq. (2.51), we obtain

$$q_{CHF} = \rho_g \Delta h_{lg} \left(\frac{2\pi\sigma}{\lambda_{KH}\rho_g}\right)^{1/2} \frac{\pi a^2 \lambda_b^2}{\lambda_b^2} = \Delta h_{lg} \left(\frac{2\pi^3 a^4 \sigma \rho_g}{\lambda_{KH}}\right)^{1/2}. \tag{2.53}$$

The λ_{KH} and a must then be determined to evaluate the q_{CHF} with Eq. (2.53). From a capillary energy analysis, Rayleigh determined that for a fluid jet of diameter $2R$, the flow-critical length scale corresponding to destabilization is equal to the jet circumference, i.e., the Rayleigh wavelength $\lambda_R = 2\pi R$ [30]. Zuber then equated the Kelvin-Helmholtz and Rayleigh wavelengths as $\lambda_{KH} = \lambda_R = 2\pi R_g = 2\pi a \lambda_b$. This form still requires the proper determination of λ_b and a. In the work of Zuber, for boiling on a plain surface, the λ_b was assumed to develop from the condition of the vapor being generated on the surface but underneath the liquid pool. For a liquid-vapor interface system in which a more dense fluid is above a less dense fluid with respect to gravity, the critical instability wavelengths λ_b would arise from a balance of surface tension and buoyancy and would result in either the most critical (largest disturbance) or most dangerous (fastest growing disturbance) Rayleigh-Taylor instability wavelength, $\lambda_{RT,c}$ or $\lambda_{RT,d} = 3^{1/2}\lambda_{RT,c} = 3^{1/2}(2\pi)\{\sigma/[g(\rho_l - \rho_g)]\}^{1/2}$. After separately substituting both of these wavelengths into Eq. (2.53), Zuber simplified

the two results into his well known relation for the critical heat flux from plain surfaces by compromising on an intermediate value of $\lambda_b = (9/2\pi)\lambda_{RT,c}$. He then set $\lambda_{KH} = 2\pi a\lambda_b = 9a\lambda_{RT,c}$ to obtain,

$$\frac{q_{CHF,Z}}{\rho_g^{1/2}\Delta h_{lg}[\sigma g(\rho_l - \rho_g)]^{1/4}} = \frac{\pi}{24}, \tag{2.54}$$

where, also for simplicity, he chose $a = 1/4$. Lienhard and Dhir [40] argued from experimental observation that the $\lambda_{RT,d}$ would be the dominating flow-critical length scale along the surface, and that for infinite surfaces, these waves would continue into the vapor channels, thus effecting the destabilization of the channel walls before the Rayleigh waves. They suggested as a better choice to set $\lambda_b = \lambda_{KH} = \lambda_{RT,d} = 3^{1/2}\lambda_{RT,c}$ resulting in a value 1.14 times higher than that predicted by Eq. (2.54).

These determinations of λ_b ignore the presence of any protuberances into the liquid-vapor interface that might delay the development of the λ_{RT}, thus prolonging the wetting of the surface by allowing the liquid to break through. We hypothesize that modulation of the porous-layer thickness (i.e., introduction of protuberances), imposes a geometrically determined critical length scale λ_m, corresponding to the modulation wavelength, that supersedes the dependence on the Rayleigh-Taylor wavelength and extends the hydrodynamic liquid-choking limit. The modulation therefore delays surface dryout and extends the q_{CHF} to where a stable flow-critical wavelength can be established between two protuberances. Figure 2.9 shows a rendering of the physical model for the hydrodynamic instability limit to liquid reaching the surface for both the porous-layer coating and a plain surface. Measurements of the q_{CHF} from a plain surface performed for this study had good agreement with Eq. (2.54). Therefore, using Zuber's approach with $a = 1/4$ and setting

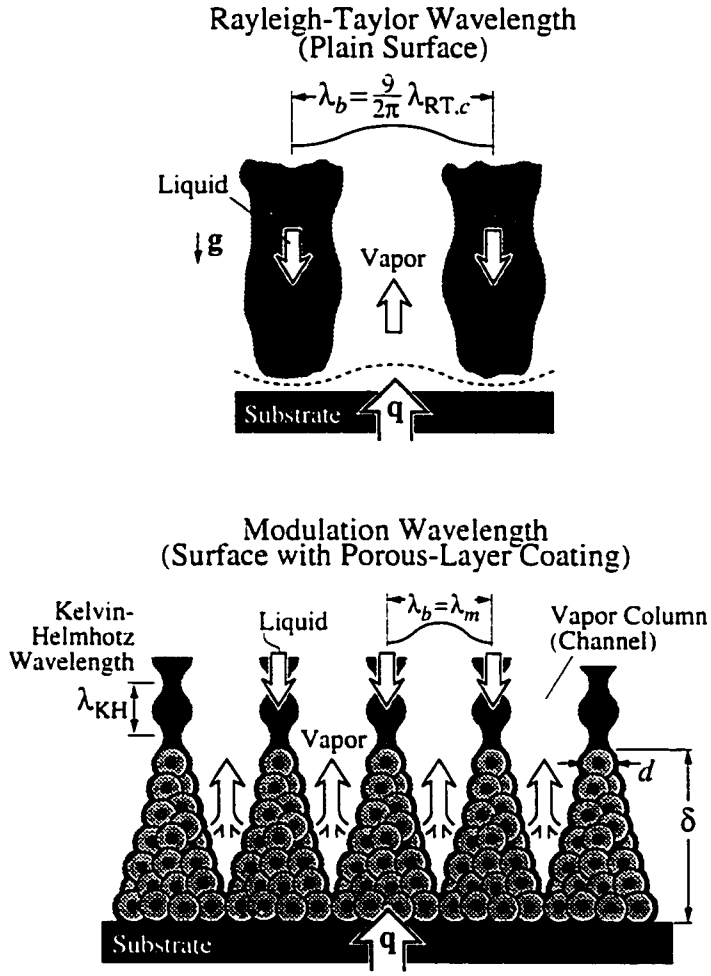

Figure 2.9: A rendering of the physical model of the hydrodynamic instability limit to liquid reaching the surface for a plain surface and a modulated porous-layer coating.

$\lambda_{KH} = 2\pi a\lambda_b = 2\pi a\lambda_m$, Eq. (2.53) then becomes

$$\frac{q_{CHF,h}}{\frac{\pi}{24}\rho_g^{1/2}\Delta h_{lg}[\sigma g(\rho_l - \rho_g)]^{1/4}} = (\frac{9}{2\pi}\frac{\lambda_{RT,c}}{\lambda_m})^{1/2} = \frac{3[\frac{\sigma}{g(\rho_l - \rho_g)}]^{1/4}}{\lambda_m^{1/2}}, \qquad (2.55)$$

or more simply

$$q_{CHF,h} = \frac{\pi}{8}\Delta h_{lg}(\frac{\sigma\rho_g}{\lambda_m})^{1/2},$$

where the subscript h distinguishes this q_{CHF} as the hydrodynamic liquid-choking limit (as opposed to the viscous-drag liquid-choking limit), and where $\lambda_b = \lambda_m$ is now assumed to be determined by the dominating mechanism for determining the vapor-escape spacing along the surface. For the porous-layer coated surface, λ_m corresponds to the macro-scale geometry (i.e., a modulation wavelength) of the modulated porous-layer coating.

Figure 2.10 shows the variation of $q_{CHF,h}$ with λ_m following Eq. (2.55) for pentane as the working fluid. The upper limit of λ_m for it to still affect the $q_{CHF,h}$ is $\lambda_m \rightarrow (9/2\pi)\lambda_{RT,c}$, because this is where the $q_{CHF,h} \rightarrow q_{CHF,Z}$. The $q_{CHF,h}$ increases proportionally with $\lambda_m^{-1/2}$ as λ_m is reduced from $(9/2\pi)\lambda_{RT,c}$. There exists a λ_m for optimum $q_{CHF,h}$, below which a larger λ_b will begin to develop over the top of the protuberances resulting in a decrease in the q_{CHF}. The optimum λ_m is considered to be a function of a liquid-column (channel) curvature limit which depends on the porous-medium particle diameter d, fluid properties, and coating thickness δ. In the limit of $\lambda_m \rightarrow d$, the modulation effectively vanishes and the coating becomes a uniform porous-layer coating with its accompanying, lower enhancement in q_{CHF}. Determination of the optimum λ_m is yet to be done.

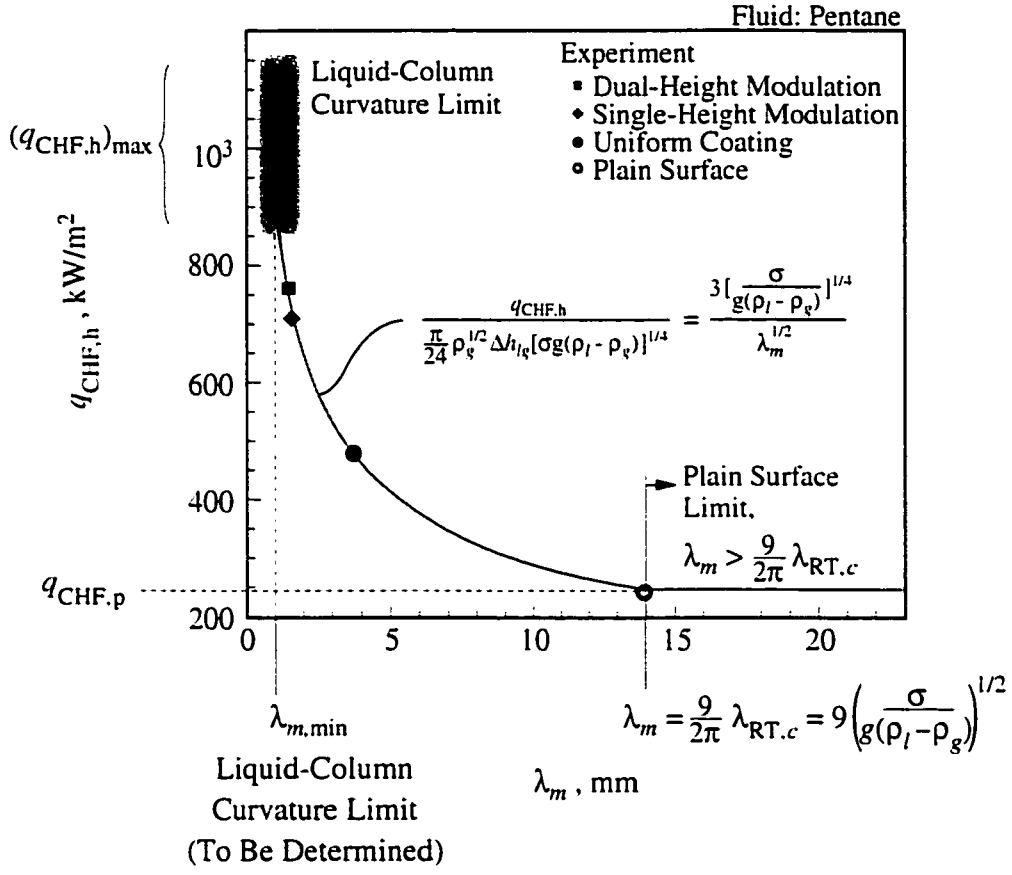

Figure 2.10: Predicted $q_{CHF,h}$ as a function of modulation wavelength λ_m.

CHAPTER III

EXPERIMENT

As mentioned in Chapter 1, a method for fabricating the porous-layer coatings with designed modulation was developed. Coatings were fabricated from monosized, spherical copper particles and were applied to a solid, planar copper test surface of $d = 5.08$ cm. Different porous layers were constructed with various porous-layer overall thicknesses ranging between 1 to 9 particle diameters, and various modulations creating uniformly spaced hexagonal unit cells ranging in size from 5 to 15 particle diameters. Only the two modulated porous-layer coatings exhibiting the best enhancement are presented in detail here. The results from the other tests and their interpretations follow at the end of this chapter. The two are:

(i) A coating of single-height modulated conical stacks fabricated with $\delta = 6d_p$, and $\lambda_b = 5d_p$ ($d_p = 200$ μm). This surface is shown in Figure 3.1.

(ii) A coating of dual-height modulated conical stack groups consisting of a tall stack of $\delta = 9d_p$ surrounded by six shorter stacks of $\delta = 5d_p$, and a peak-to-peak tall-stack spacing of $\lambda_b = 8d_p$ ($d_p = 200$ μm). This surface is shown in Figure 3.2.

Experiments were performed at atmospheric pressure using pentane as the liquid and copper as the surface and coating-particle material. The pentane satu-

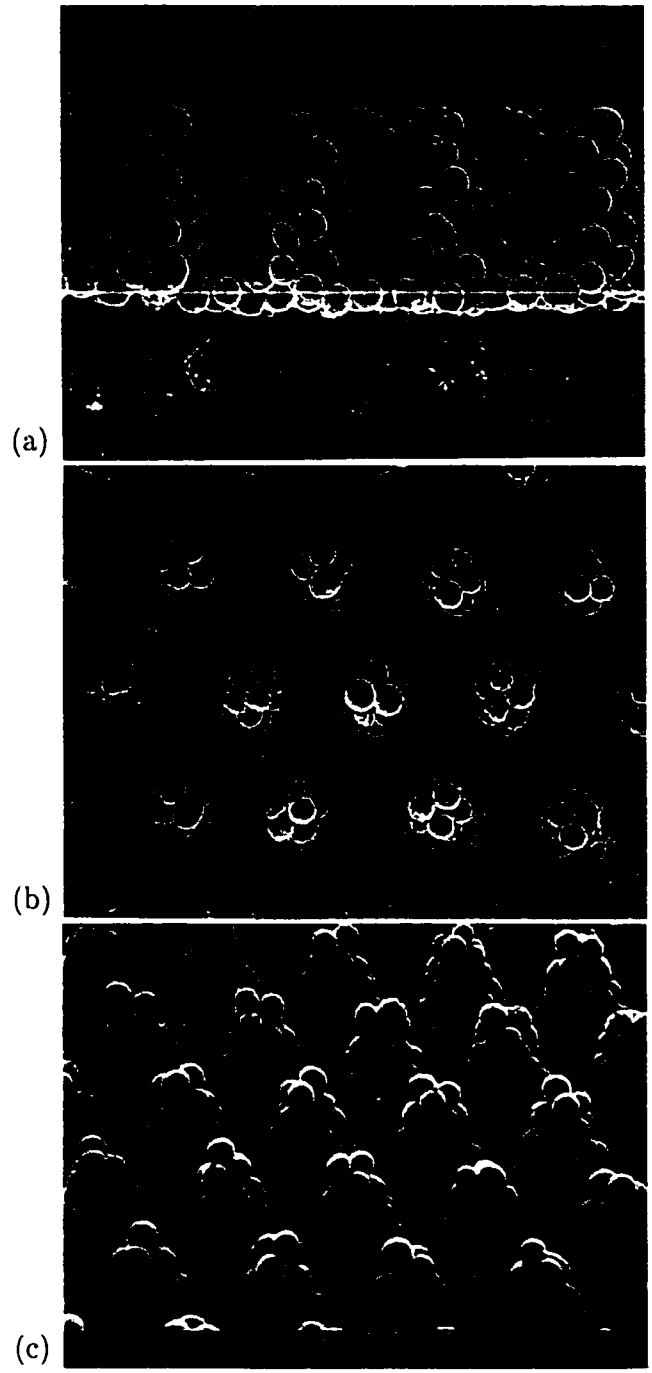

Figure 3.1: SEM of single-height, modulated porous-layer coating showing a) the side view, b) top view, and c) the perspective view. The porous-layer contains spherical copper particles of diameter $d = 200$ μm molded into conical stacks.

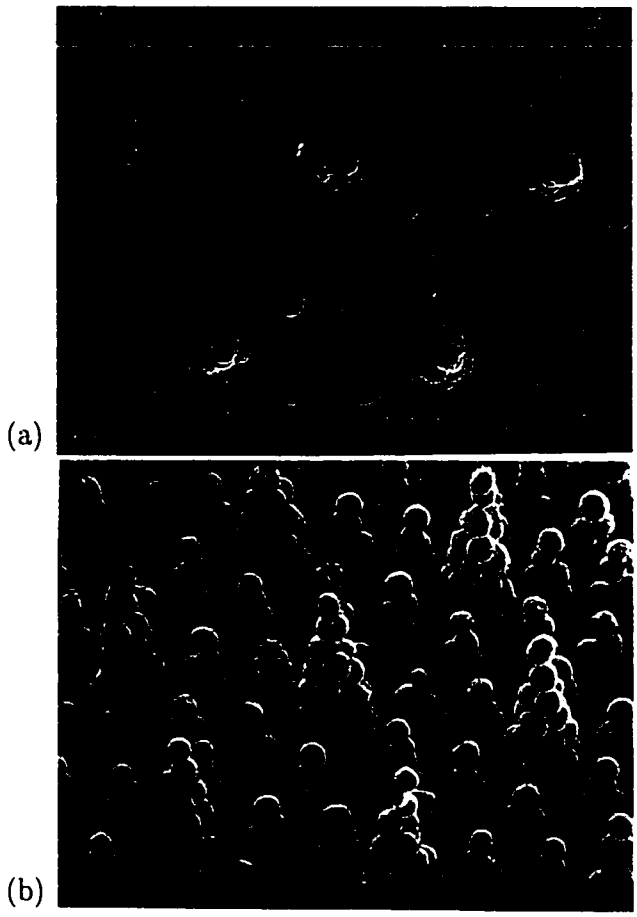

Figure 3.2: SEM of dual-height, modulated porous-layer coating showing a) top view, and b) the perspective view. The porous-layer contains spherical copper particles of diameter $d = 200$ μm molded into conical stacks.

ration properties used are listed in Table 3.1. To better approximate the boiling from an infinite flat surface, a short glass cylinder was positioned in the liquid pool around the circular test surface to prevent lateral entrainment of liquid due to the buoyant convection of the vapor. Joulean heaters were used to heat an insulated copper thermal mass to which the test surfaces were attached. The Q and $T_s - T_{lg}$ were measured after the system reached quasi-steady state conditions at intervals of increasing heat input. The q_{CHF} was said to have occurred at the last quasi-steady state measurement interval before the transition to film boiling was observed.

Table 3.1: Thermophysical properties of saturated pentane at 1 atm [48].

M	72.151 kg/kmol
T_{lg}	36.05℃
ρ_l	610.2 kg/m^3
ρ_g	3.00 kg/m^3
Δh_{lg}	358.2 kJ/kg
σ	0.0143 N/m
μ_l	1.96×10^{-4} kg/m-s
μ_g	6.9×10^{-6} kg/m-s
k_l	0.107 W/m-K
k_g	0.0167 W/m-K
$c_{p,l}$	2340 J/Kg-K
Pr	4.29

3.1 Porous-Layer Coating

3.1.1 Design Objective

As stated, modulated porous-layer coatings are coatings with periodic, designed variations in layer thickness δ. The modulation is imposed to create alternating regions of low resistance to vapor escape and high capillary-assisted liquid draw. The objective in design is to then develop a way of creating repeatable and uniform modulations in a this porous coating while controlling the modulation geometry.

3.1.2 Fabrication of Coating

The porous-layer coatings used in this study are made of spherical copper particles screened between size 80 mesh (180 μm) and 60 mesh (250 μm) sieves to supply an nearly uniform particle diameter of 200 μm. Open-faced graphite molds are machined to provide a 3-dimensional negative image of the desired coating modulations, enabling the creation of certain opened, controlled-shaped voids or structures within the layer. The process for surface fabrication is as follows. The particles are poured into the mold and shaken level. The test piece is then placed inverted onto the powders so that gravity holds the test surface in contact with the particles while the mold holds the particles in the shape of the desired modulated surface. The mold, particles, and test piece are then placed into a tube furnace with a reducing atmosphere. While in the furnace, the particles are diffusion sintered together and to the test surface creating the porous-layer coating.

The modulation in the graphite mold was machined using either dicing blades or single-flute pointed drill bits with a $\theta = 20°$ taper. Mechanical limitations of the strength of the drill bit prohibited the use of drill bits with smaller included-angle tapers. Modulation size limitations were also inherent in the ability of the graphite

to resist flaking or chipping during machining (i.e., high aspect ratio or very thin graphite walls in the mold were not possible). These manufacturing restrictions, as well as the geometric restrictions arising from the modulation structures being nearly the same order in size as the spherical particle diameters, placed restrictions on the possible modulation length scales and designs that could be fabricated with this method. An additional and unnecessary restriction was imposed such that the modulation be divisible into repeated unit cells to simplify analytical modeling.

The resulting fabricated modulations consisted of either particle walls in a "waffle" pattern or of conical "stacks" of particles arranged in either square or hexagonal arrays across the surface. Preliminary results indicated that coatings consisting of the particle stacks provided better performance. Therefore, the predictions of the results from these coatings were a major focus of this study and a single particle stack was used as the domain for the analytical model.

3.2 Experimental Apparatus

The experimental apparatus is shown in Fig. 3.3. A solid copper cylinder is used as a thermally massive base to supply heat to the testing surface. The top of the base is machined with a male screw thread for attachment of test surface pieces. A 3.8 cm diameter flat surface is left on the top of the thread for thermal contact between the base and the test pieces. The large thermal mass of the base provides a thermal inertia that allows the q_{CHF} through the test surface to be observed while afterwards allowing enough time to power-down the system before the solid temperature reaches destructive levels.

The base cylinder is heated by a 1.3 kW cartridge heater, and by a 1 kW band

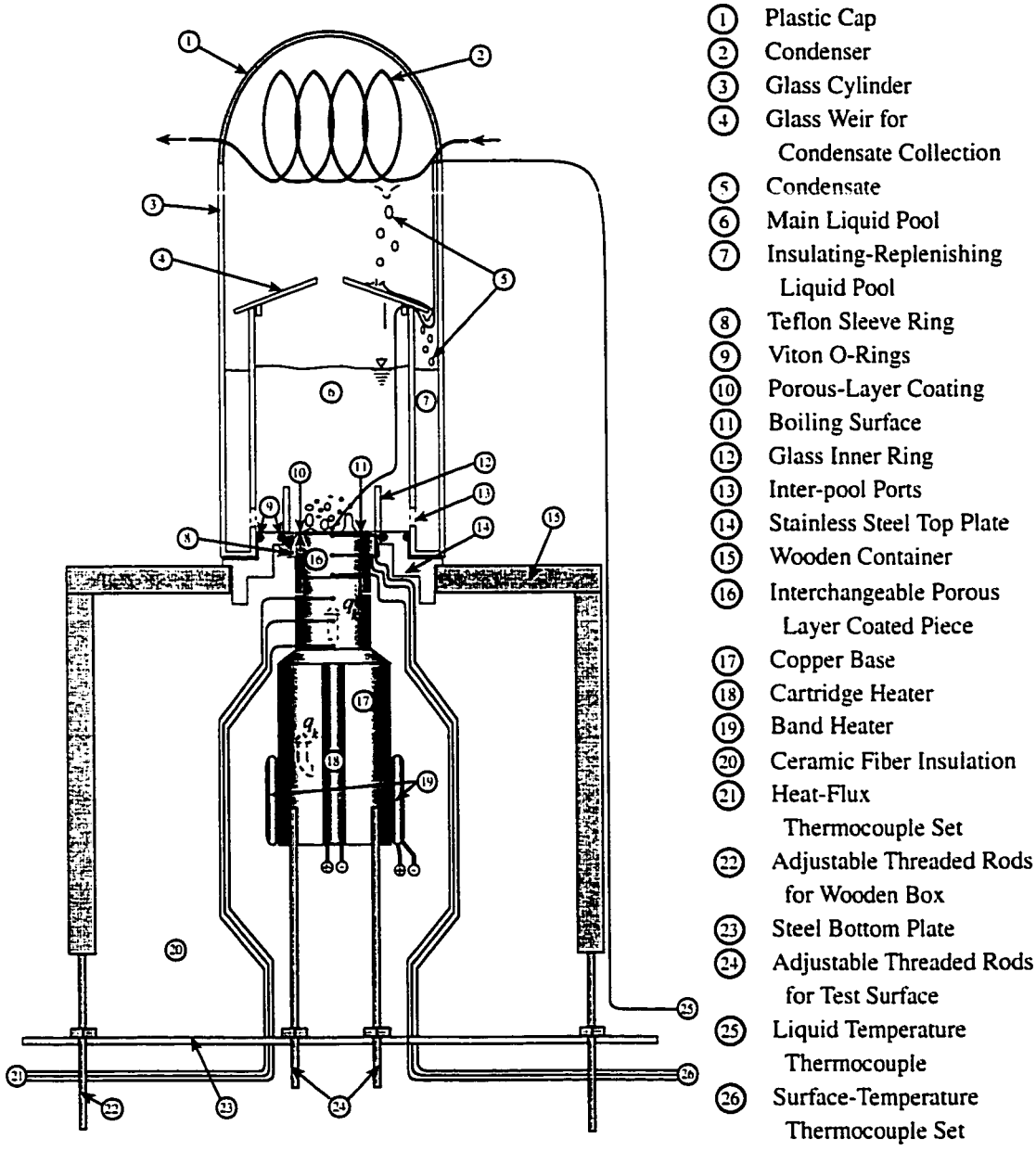

Figure 3.3: Schematic of the experimental setup.

heater wrapped circumferentially around the lower half of the base. The cylindrical base is surrounded on the sides and bottom by a ceramic fiber insulation and then enclosed in a wooden container. A stainless steel top plate is attached to the top of the wooden container. The test piece is extended through this top plate exposing the test surface to the fluid. The copper base and the wooden container are mounted independently on a steel bottom plate using threaded rods. After a test piece is screwed onto the copper base, the threaded rods are adjusted at the bottom plate until the test piece is horizontally level with, and extending through, the stainless steel top plate.

The test pieces are constructed from a 5.08 cm diameter copper cylinder. They measure 3.8 cm in height with a screw thread machined axially into the bottom. The test pieces are screwed onto the base such that the bottom of the pocket-well of the thread in the test piece seats flush with the flat surface on the top of the male thread of the base. Thermally conductive silver grease is used between the test piece and base contact surfaces to reduce the thermal contact resistance. The porous-layer coatings are applied onto the top 5.08 cm diameter area of the test piece using solid-phase diffusion sintering methods. A rectangular cross-section, circular Teflon sleeve is placed around the circumference of the test piece top-flush with the testing surface to reduce boiling from the sides of the test piece. The sleeve is sealed to the test piece with high-temperature silicone putty to prevent leaking. A Viton O-ring is used to seal between the Teflon sleeve and the stainless steel top plate. The remaining crevice between the Teflon sleeve and the test piece does provide a nucleation site for boiling, but visual observations revealed that the rate of bubble formation (and therefore the amount of heat flux flowing to the crevice) was much smaller than that for the majority of the porous-coated surface. Therefore the effect of boiling from

the crevice was considered to be within the experimental error.

A Pyrex glass reservoir was fabricated from two concentric cylinders (one having a 8.9 cm ID and an 18 cm length, and the other having a 12.0 cm ID and 30 cm length) fused at the bottom. This glass reservoir is positioned upon the top plate as shown in Figure 3.3 where the inner cylinder is sealed to the stainless steel plate with a Viton O-ring. The volume inside the inner cylinder constitutes the main liquid pool, in which the boiling takes place. The annular volume between the two cylinders constitutes the insulating-replenishing liquid pool. A tape/guard heater (not shown in the Figure 3.3) is wrapped around the outer cylinder to ensure uniform saturation temperatures within the liquid. The top of the glass reservoir is closed with a plastic cap through which runs a copper coil condenser. A shallow, conical shaped Pyrex glass weir is used to direct the falling condensate from the condenser into the insulating-replenishing pool where it is reheated to its saturation temperature. The liquid is allowed to flow from the insulating-replenishing pool into the main pool through 6 circumferentially spaced inter-pool ports. A Pyrex glass inner ring (3.8 cm length, 5.3 cm ID) is placed in the main liquid pool, on the top plate, and around the test surface to prevent liquid cross flows and reduce entrainment.

3.3 Experimental Procedure

Power is turned on and increased until boiling initiates. The liquid is boiled in the lower end of the nucleate boiling regime for 4 to 6 hours to purge any dissolved gases. The surface superheat and heat flux are then measured. The power is then incrementally increased and the system is allowed to reach quasi-steady state conditions. Quasi-steady state conditions are considered to be reached when the

average temperature of each of the thermocouples appears steady (within ±0.1℃) for at least 120 seconds. The power is then again incrementally increased and the same procedure is followed. When the critical heat flux is surpassed, the system is seen to exhibit film boiling on the surface and the temperatures in the copper test piece quickly begin to rise. As soon as this occurs, power is turned off and the last quasi-steady state heat flux data point is taken as the critical heat flux for that surface. All heat flux measurements are taken for increasing increments and the effects of hysteresis are not explored

3.3.1 Data Acquisition

Seven Type E thermocouples are positioned as shown in Figure 3.3 and are used to measure the temperatures and heat flux through the system. The six thermocouples positioned in the copper base and test piece, labeled as 20 and 25 in the figure, are potted with a copper-oxide ceramic into holes such that the thermocouple beads are aligned along the axial center line. The three thermocouple beads in the copper base are located at 14.0 cm, 15.7 cm, and 17.5 cm above the bottom and are referred to as the heat-flux thermocouple set. The first and third thermocouple temperature readings of the heat-flux set are used in conjunction with Fourier's Conduction Law to determine the heat flux to the test surface. The three thermocouple beads in the test piece are located at distances of 2.15 cm, 1.15 cm, and 0.15 cm below the test surface before coating and are referred to as the surface-temperature set. The readings of the first thermocouple (located at $x = 2.15$ cm) of the surface-temperature set and the determined heat flux are used with Fourier's Conduction Law to estimate the surface temperature at the testing surface under the porous-layer coating. The seventh thermocouple is located in the main liquid pool nearly

2 mm above the center of the porous-layer coating. This thermocouple is used to monitor the bulk liquid temperature above the surface to ensure that the saturation temperature is maintained.

3.3.2 Measurement Uncertainty

The measurement uncertainties were evaluated using the method of Kline and McClintock [49]. Property uncertainties were estimated to be 0.5 percent, thermocouples uncertainties to be 1.7℃, and length measurement uncertainties to be 0.05 cm.

The uncertainty in the heat flux, U_q, was evaluated as

$$U_q = q[(\frac{U_k}{k_s})^2 + (\frac{U_{T_1}}{\Delta T})^2 + (\frac{U_{T_3}}{\Delta T})^2 + (\frac{U_{x_1}}{\Delta x})^2 + (\frac{U_{x_2}}{\Delta x})^2]^{1/2}. \tag{3.1}$$

For typical values at the critical heat flux point of a modulated porous-layer coated surface, this estimates the percent uncertainty in the critical heat flux to be

$$\frac{U_q}{q} = [(0.005)^2 + 2(\frac{1.7℃}{66℃})^2 + 2(\frac{0.05\text{ cm}}{3.56\text{ cm}})^2]^{1/2} * 100\% = 4.2\%. \tag{3.2}$$

Note that the uncertainty increases with decreasing heat flux due to the smaller ΔT.

The percent uncertainty of the extrapolated surface temperature was similarly found to be

$$\frac{U_{T_s}}{T_s} = [(\frac{U_k}{k_s})^2 + (\frac{U_q}{q})^2 + (\frac{U_{T_1}}{\Delta T})^2 + (\frac{U_{x_1}}{\Delta x})^2]^{1/2} \tag{3.3}$$

$$= [(0.005)^2 + (0.042)^2 + (\frac{1.7℃}{40℃})^2 + (\frac{0.05\text{ cm}}{2.15\text{ cm}})^2]^{1/2} * 100\% = 6.4\%. \tag{3.4}$$

CHAPTER IV

Results and Discussion

4.1 Measurements

Repeatable results for a number of surfaces with various porous-layer coating modulations have been obtained for the heat flux q versus the surface superheat $T_s - T_{lg}$ up to the critical heat flux q_{CHF}. Figure 4.1 shows four experimentally obtained curves: the two reported modulated porous-layer coatings, a uniform porous-layer coating, and a plain, polished surface. Table 4.1 lists the experimental results for the q_{CHF} points of these four curves.

Table 4.1: Measured q_{CHF} and the corresponding $T_s - T_{lg}$ for the surfaces shown in Fig. 4.1.

	$(T_s - T_{lg})_{\mathrm{CHF}}$, °C	q_{CHF}, kW/m^2
Dual Height-Modulation	22.0 ± 1.4	762 ± 32
Single-Height Modulation	16.4 ± 1.0	712 ± 30
Uniform Coating	22.2 ± 2.1	480 ± 22
Plain Surface	34.2 ± 4.0	245 ± 13

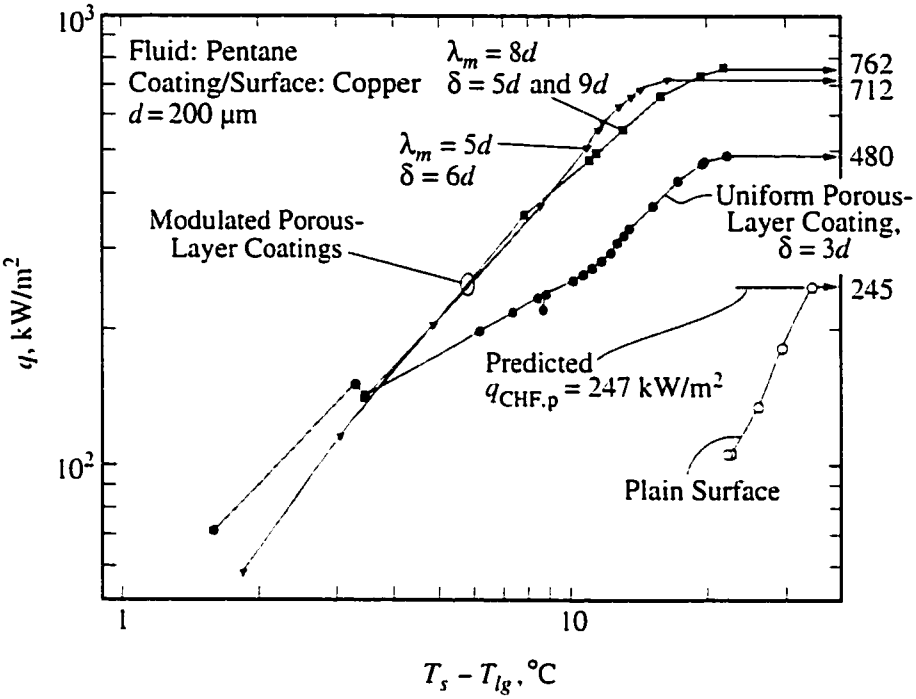

Figure 4.1: Measured pool-boiling heat transfer from porous-layer coated surfaces.

The measurement of the plain surface critical heat flux was $q_{CHF} = 245$ kW/m^2. The uniform porous-layer coating provided a two-fold increase in the critical heat flux, $q_{CHF} = 480$ kW/m^2, in agreement with results for similar coatings found by other researchers [27, 20, 15, 16, 22].

The results for the modulated porous-layer coatings provided an additional single-fold increase in the q_{CHF} over that of a uniform coating, while further decreasing the surface superheat at high heat fluxes during the nucleate boiling regime. The single-height modulated porous layer coating provided a $q_{CHF} = 712$ kW/m^2. The dual-height modulated porous layer coating exhibited the greatest enhancement in the q_{CHF} over that of the plain surface, $q_{CHF} = 762$ kW/m^2, an enhancement of nearly three times. For both modulated porous-layer coatings, the q versus $T_s - T_{lg}$ profiles are nearly equal and are an order of magnitude lower than the plain surface $T_s - T_{lg}$.

4.2 Predicted Wetted-Surface Regime and Viscous-Drag Liquid-Choking Limit

The measured value of $q_{CHF} = 245$ kW/m^2 for the plain surface was found to be in excellent agreement with that predicted by Eq. (2.54) as $q_{CHF,P} = 247$ kW/m^2. The liquid and vapor exchange in and above a uniform coating, i.e., not having preferential paths provided by modulation of the coating or by some other means, would be characterized by a random distribution of vapor escape from a fraction of the pores into the liquid pool above the layer. It has been suggested that a corresponding $\lambda_m = \lambda_u$ for a uniform coating could be determined using statistical empiricism for the vapor escape locations, along with a means of accounting for the liquid-vapor counterflow within the layer such as a percolation theory or the concept

of a breakthrough pressure [21]. Using the concept of the breakthrough pressure along with a statistical pore-size distribution for a wide range of experimental data, Polezhaev and Kovalev [21] modified the hydrodynamic Zuber theory to suggest an expression with two empirical constants for the thin uniform porous-layer coating critical heat flux, $q_{\mathrm{CHF,u}}$, as

$$q_{\mathrm{CHF,u}} = 0.52\epsilon^{2.28}\Delta h_{lg}[\frac{\sigma\rho_l\rho_g}{(\rho_l+\rho_g)R_{br}}]^{1/2}.$$

where R_{br} is the measured breakthrough pore radius. Assuming $R_{br} = d/2$ and $\rho_l/(\rho_l+\rho_g) = 1$, this can be rewritten in the form of Eq. (2.55) as

$$\frac{q_{\mathrm{CHF,u}}}{\frac{\pi}{24}\rho_g^{1/2}\Delta h_{lg}[\sigma g(\rho_l-\rho_g)]^{1/4}} = \frac{3[\frac{\sigma}{g(\rho_l-\rho_g)}]^{1/4}}{\lambda_u^{1/2}}. \tag{4.1}$$

where

$$\lambda_u = (\frac{\pi}{5.88\epsilon^{2.28}})^2 d.$$

Note that λ_u is a function of geometry and structure only, and is independent of thermophysical properties [except whereas they might affect the R_{br} which was here assumed as $R_{br} = R_{br}(d)$]. For $d = 200$ μm and $\epsilon = 0.4$, this results in a $\lambda_u = 3.73$ mm, and a $q_{\mathrm{CHF,u}} = 478$ kW/m^2 which agrees very well with the measured value of $q_{\mathrm{CHF}} = 480$ kW/m^2 shown in Fig. 4.1. The agreement is surprising considering that R_{br} was approximated and not measured. Nevertheless, the excellent agreement between the predicted $q_{\mathrm{CHF,h}}$ and the measured q_{CHF} for the plain and uniformly coated surfaces lends credence to the hydrodynamic model as a prediction tool for the q_{CHF}.

For the dual-height modulation results shown in Fig. 4.1, with $q_{CHF} = 762$ kW/m^2, the corresponding λ_m predicted from Eq. (2.55) is 1.46 mm, in good agreement with the designed modulation wavelength between the tall center stacks of $\lambda_m = \lambda_b = 8d = 1.6$ mm. Note that the side-to-side distance of the top spherical particles of two adjacent stacks is $\lambda_b - d = 1.4$ mm, and that the predicted λ_m falls between the side-to-side and center-to-center distances.

For the single-height modulation results shown in Fig. 4.1, with $q_{CHF} = 712$ kW/m^2, the corresponding λ_m predicted from Eq. (2.55) is near 1.68 mm, which is greater than the designed $\lambda_b = 5d = 1$ mm. Note though that the next larger length scale across the coating, the distance from one stack to, not one of the six adjacent nearest, but one of the six next nearest stacks is $\lambda_m = (3)^{1/2}\lambda_b = 1.73$ mm, with a side-to-side distance of the top spherical particles of 1.53 mm. Within this theory, this would indicate that a stable wavelength has developed between a pair of nearest, but not adjacent, stacks and extended in between the two adjacent stacks separating them, where the two adjacent stacks do not provide interference destabilizing the interfacial wave.

The measured results for both cases are therefore considered to correlate well with that predicted by Eq. (2.55) and shown in Fig. 2.10 as a function of a geometric length scale of the coating. It is, however, important to note that the correct length scale is not always the most obvious one, as shown in the case of the uniform-height stacks. The selection process for the appropriate length scale determining the hydrodynamic liquid-choking limit needs further examination. To determine when side obstacles would create an interference destabilizing a developing interfacial wavelength, the radius of action (magnitude) of the wave must be determined. This is beyond the scope of the current work and is left for future consideration. Note,

though, that in the case of the dual-height coating, the presence of the short stacks introducing interference would explain why the critical heat flux corresponded to the spacing between two nearest tall stacks, instead of the next nearest.

4.3 Predicted Boiling Curve of Capillary Surfaces

The viscous-drag model allowed for the prediction of the wetted-surface regime up to and including the $q_{\mathrm{CHF,v}}$. The slope of the predicted q versus $T_s - T_{lg}$ curve for the wetted surface regime is considered to be in fair agreement with the measurements. Both the prediction and measurements are shown in Fig. 4.2. For a given surface heat flux, the model can be seen to over predict the $T_s - T_{lg}$, but it is still considered to be in fair agreement with the measurements. At $q_{\mathrm{CHF}} = 712$ kW/m^2, measured for the single height modulation, the measured $T_s - T_{lg} = 16.36$°C. The model predicts a value of $T_s - T_{lg} = 22.3$°C, a difference of 36%.

The $q_{\mathrm{CHF,v}}$ is dependent on the liquid velocity distribution, the particle size d (through the coating thickness $\delta(d)$, and the permeability, K), the particle and liquid thermal conductivities k_s and k_l, and the porous-layer macrostructure (i.e., the λ_b and the modulation geometry of the cones, etc.). An analytical expression was given in Eq. (2.48) to approximate the numerical results. The dependence on the included cone angle has been included through the use of an empirical coeffienct C_θ that accounts for the diverging flow area through the flow corridor and the corresponding increase in viscous-drag resistance through the artery region. This was found to be nearly independent of d and was shown in Fig. 2.7. The dependence on particle diameter is shown in Eq. (2.44) where $\delta = \delta(d)$. Here it was noted that as the diameter of the system decreased, the inertia term (i.e., $\mathrm{We}_{K^{1/2}}$) in Eq. (2.42) became negligible and the solution became Darcy (or viscous) limited. This is shown in

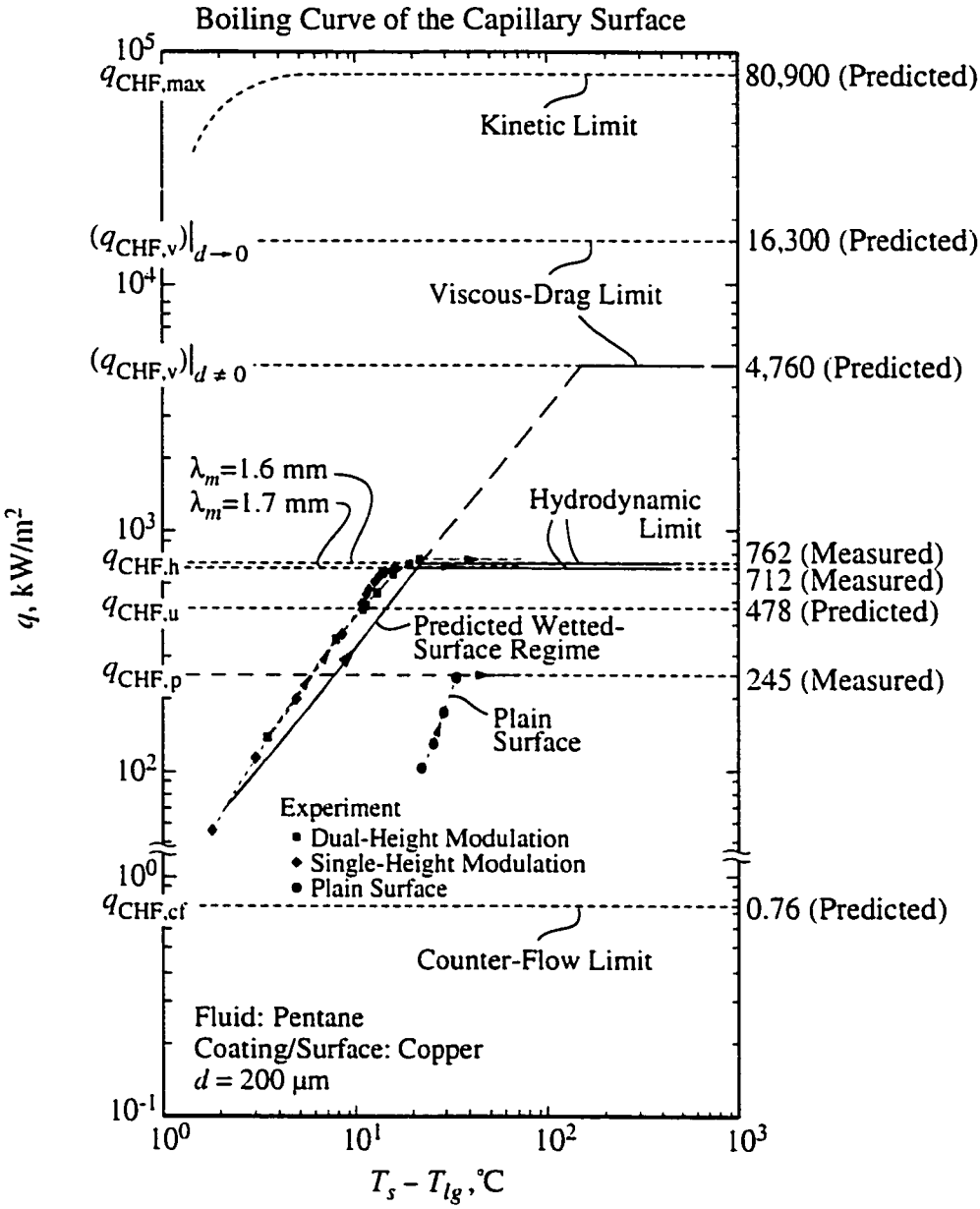

Figure 4.2: Comparison of the measured and predicted pool-boiling heat transfer rate from modulated porous-layer coated surfaces.

Fig. 4.3, for $C_\theta(\theta = 20°) = 0.4$, along with the Darcy limit and the prediction of $q_{CHF,h}$ from Eq. (2.55). Variations in these parameters can raise or lower the $q_{CHF,v}$, as well shift the q versus $T_s - T_{lg}$ curve left or right.

The predicted $q_{CHF,v}$ for a particle stack with $d = 200$ μm and $\delta = 6d$ was $q_{CHF,v}$ =4,760 kW/m^2. This is higher than both the predicted $q_{CHF,h}$ and the measurements by an order of magnitude. A more realistic flow distribution would be expected to increase the liquid-flow resistance and reduce the predicted viscous-drag liquid-choking limit, but it is not believed that the $q_{CHF,v}$ would actually fall below the predicted $q_{CHF,h}$ for these coatings.

The formulation of the $q_{CHF,v}$ assumed complete phase separation within the stack. If vapor-liquid counter-flow was considered to occur within the stack, the viscous liquid-flow resistance would increase substantially for the same surface heat flux, q. Additionally, the liquid-flow resistance also increases with the porous-layer thickness. Therefore a deep uniform porous-layer, in which there was liquid-vapor counterflow, would be expected to have a high liquid-flow resistance and to exhibit a low counterflow critical heat flux, $q_{CHF} = q_{CHF,cf}$. The expression for $q_{CHF,cf}$ from Udell [26] was given in Eq. (1.1). For pentane boiling in a deep porous layer consisting of particels of $d = 200$ μm and $\epsilon = 0.4$, this results in a $q_{CHF,cf} = 759$ W/m^2, three orders of magnitude less than for the thin modulated porous-layer coatings.

Figure 4.2 shows the experimental results plotted against the numerical predictions. The predicted $q_{CHF,h}$, from Eq. (2.55), for the λ_m suggested by each of the two modulated porous-layer coatings, is shown along with the prediction of the q versus $T_s - T_{lg}$ curve up to the $q_{CHF,v}$ from the viscous-drag numerical model for the uniform-height coating.

By our theory, the surface q versus $T_s - T_{lg}$ would follow the viscous-drag

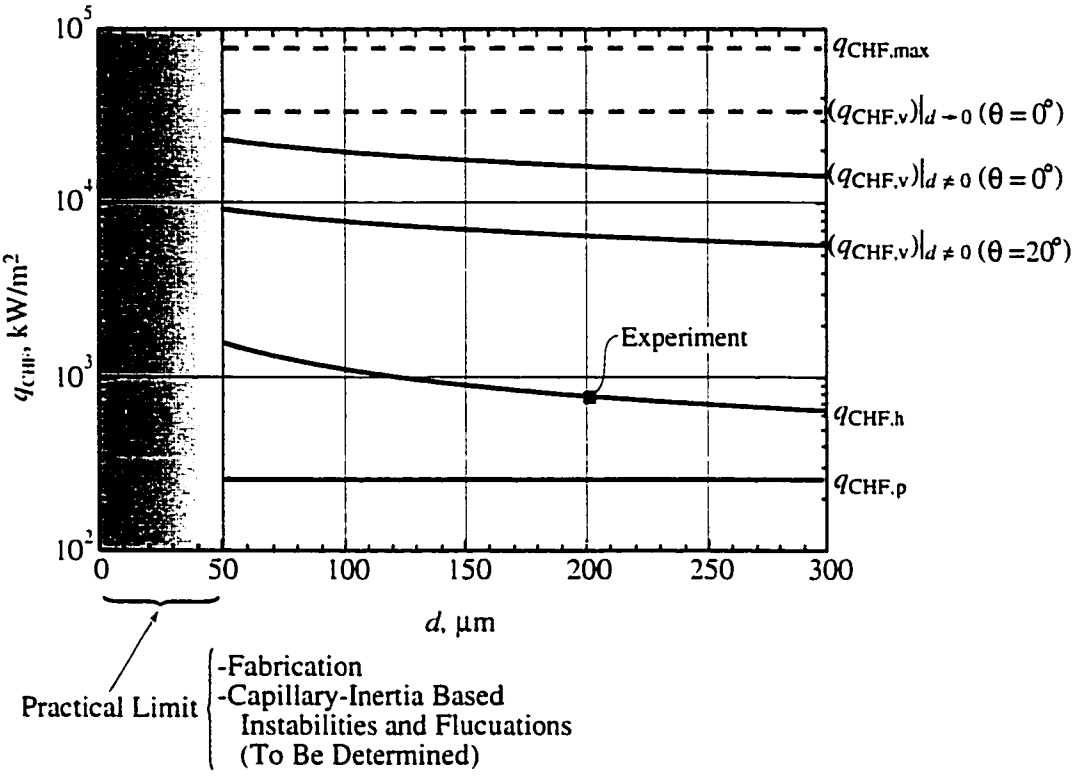

Figure 4.3: Comparison of predicted hydrodynamic and viscous-drag liquid-choking limits as a function of d. Also shown is the Darcy limit for the viscous-drag liquid-choking limit, and the experimental result for the dual-height modulated porous-layer coating.

predicted q versus $T_s - T_{lg}$ until either of the two liquid-choking limits occurs. In this case the predicted viscous-drag liquid-choking limit is much higher than the predicted hydrodynamic limit, i.e., $q_{\mathrm{CHF,v}}$ =4,760 kW/m^2-K $\gg q_{\mathrm{CHF,h}} = 762$ kW/m^2-K. Therefore this coating is predicted to be hydrodynamically limited and the portion of the predicted q versus $T_s - T_{lg}$ for $q_{\mathrm{CHF,h}} < q < q_{\mathrm{CHF,v}}$, depicted by the long-dashed line, is not observed. The experimental boiling curve is then predicted to follow the solid lines as shown in Fig. 4.2.

4.4 Analysis and Optimization Considerations

Two types of optimization of modulated porous-layer coatings can be considered, namely, reduction of $T_s - T_{lg}$ and increase of q_{CHF}.

The modulated porous-layer coating is an example of an artery-evaporator system as described above. The concept of an artery-evaporator system in itself is only limited by the viscous-drag liquid-flow resistance. It is the macrostructure shape of the system and the locations and means of vapor escape from the system that can further limit the q_{CHF}. Optimization of the q_{CHF} can be achieved by minimizing the flow resistance to vapor escape from the surface, i.e., maximizing the liquid-choking limit. In the case of the uniform and modulated porous-layer coatings presented here, the vapor escapes by buoyancy into the liquid pool, and thus places the hydrodynamic limit on the liquid supply to the artery.

For hydrodynamically limited surfaces, $q_{\mathrm{CHF}} = q_{\mathrm{CHF,h}}$ increases with decreasing λ_m down to a theoretical liquid-curvature limit $\lambda_{m,\mathrm{min}}$, below which, the $q_{\mathrm{CHF,h}}$ would decrease from the maximum possible value towards the q_{CHF} of a surface with a uniform porous-layer coating. The maximum $q_{\mathrm{CHF,h}}$ is a function of the fluid properties and the coating macrostructure, and therefore would indicate the optimum

pool boiling q_{CHF} that can be achieved by an opened-modulation porous-layer coating in which the vapor escapes back through the liquid in a buoyant counterflow. The minimum λ_m has not yet been determined or experimentally verified and is left for future consideration. It is possibly related to the decreasing radius of curvature across two modulation peaks as the modulation wavelength is decreased. This would determine a minimum stable bubble departure diameter, dependent on surface tension, for the vapor to escape into the liquid pool. If this bubble diameter is near the λ_m, then there will be increased resistance to the vapor leaving the porous layer from in between stacks creating a vapor accumulation near the surface that would increase the liquid-flow resistance to the incoming liquid supplying the artery.

Since the present surfaces appear to be hydrodynamically limited, discussion of optimization of the $q_{\mathrm{CHF},v}$ appears to be academic. But if a means of removing the hydrodynamic limitation is achieved, then an artery-evaporator system optimized for the viscous-drag limit could potentially provide an additional order of magnitude increase in the q_{CHF} of an uncoated surface while still maintaining low $T_s - T_{lg}$.

The viscous-drag model does, however, allow for enhancement of the $T_s - T_{lg}$. From Eq. (2.40) the $T_s - T_{lg}$ can be seen to vary with the particle size. There must exist a minimum d below which the enhancement would degrade until at $d \to 0$ the $T_s - T_{lg} = (T_s - T_{lg})_p$. Determination of this minimum optimized d is left for future consideration. There is now a practical limitation on d imposed by fabrication. Within the proposed method of using graphite molds and sintering processes for creating a macrostructured system, it is expected that machining limitations would prevent the use of particle sizes of less than $d = O(50\ \mu\mathrm{m})$. Currently, the quality of the graphite used for the molds has limited this study to particles of $d = 200\ \mu\mathrm{m}$. Experiments on coatings made with particles of smaller d are left for future consid-

erations.

Optimization of the $T_s - T_{lg}$ can further be achieved by maximizing the rate of evaporation per unit surface area. The evaporation was noted, through predictions from the numerical viscous-drag model, to occur mainly along the sides of the lower portion of the conical particle stacks. The evaporation rate can be increased by maximizing the capillary liquid-pumping and the evaporation zone. The liquid-pumping can be increased by optimizing the balance between the opposing capillary and viscous-drag forces, i.e., by decreasing the particle size. The interfacial area of the evaporation zone can be increased either by increasing the number of particle stacks per unit surface area, or by increasing the effective conductivity, $\langle k \rangle$, of the stack to enable the heat flux to conduct further into the artery region in order to utilize more of the side area of a stack.

As a proposed (not fabricated) artery-evaporator system that would not be hydrodynamically limited, consider a porous-layer coating with modulation stacks of uniform height on top of which a thin porous layer of uniform thickness (denoted as the cover layer) is sintered. The liquid pool would then be adjacent to the top of the cover layer. This is shown schematically in Fig. 4.4 in the furthest system on the right and labeled artery-evaporator system with completely separated liquid-vapor flow paths. The cover layer in such a system would draw liquid in by capillarity. The generated vapor would then escape along the path of least flow resistance, in this case, laterally between the modulations, underneath the cover layer, and outwards to the edge of the coated surface. It is assumed that the width of the coating small enough to render the lateral vapor pressure drop negligible (i.e., no vapor-flow resistance). In this type of design, there is no liquid-vapor counterflow at the liquid entrance into the artery, and therefore the hydrodynamic liquid-choking would not occur, leaving

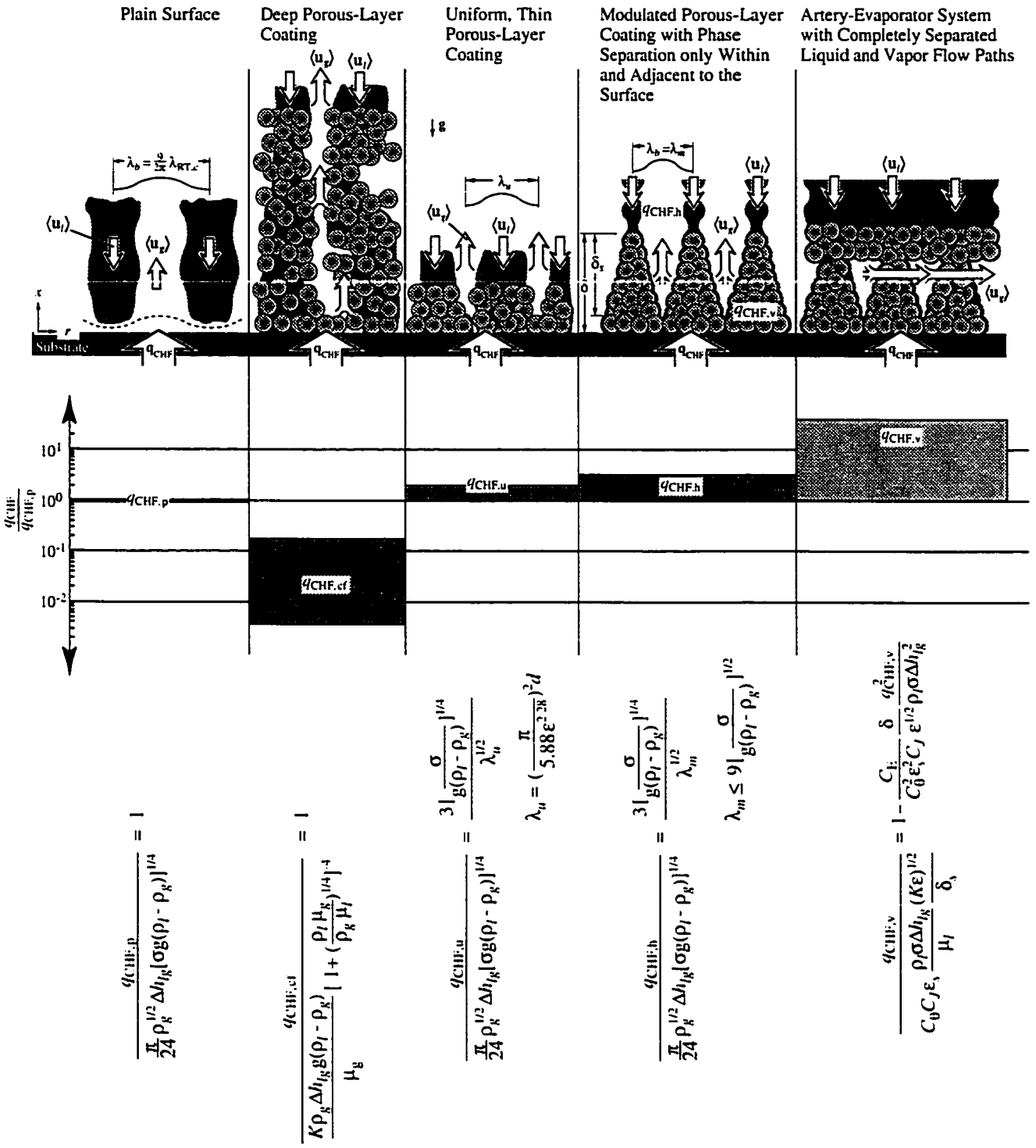

Figure 4.4: Comparison of presented liquid-choking limits along with a schematic showing the surface and/or coating structure and the liquid and vapor flow paths.

the q_{CHF} of the system to be determined by the liquid-drag viscous-choking limit. Furthermore, in such a design, the vapor no longer depends on buoyancy to remove it from the liquid entrance into the artery, and therefore the performance would be independent of gravity and orientation as long as the liquid pool was kept in contact with the cover layer. The vapor, once it reaches the side of the coated surface and leaves the porous-layer coating, could then be directed to a condenser to resupply the liquid pool. Such a system, fully utilizing the benefits of complete phase separation could potentially provide a means to realize the order of magnitude enhancement over that of a plain surface as predicted by the viscous drag model.

The proposed artery-evaporator system with completely separated liquid and vapor flow paths conceptually describes how the q_{CHF} can be increased to where they are governed by $q_{CHF,v}$ by removing the hydrodynamic liquid-choking mechanism. If the viscous-drag liquid-flow resistance can be reduced to zero, then the next limiting mechanism would be that described by the kinetic theory in Eq. (1.2). It is not possible to bypass the viscous-drag liquid-choking limit, however, with a system using a porous wick for liquid-pumping through an artery, since this type of system was shown to be viscous limited by Eq. (2.44).

CHAPTER V

Conclusions

5.1 Objective

The aim of this work was to theoretically analyze and experimentally utilize porous-layer coating to enhance pool boiling heat transfer as a specific example of an capillary artery-evaporator system.

5.2 Final Observations

Modulation of a porous-layer coating is proposed as a means to enhance the q_{CHF} while reducing the $T_s - T_{lg}$ of boiling from a plain surface.

Experiments show that porous coatings with modulation (e.g., conical macrostructures), with currently designed size, shape, and distribution, provide a 3 times increase in the q_{CHF} and a substantial decrease in the $T_s - T_{lg}$ from that for an infinite plain surface, as compared to a maximum of 2 to 2.5 times previously reported in the literature for porous-layer coatings of uniform thickness [27, 20, 15, 16, 22].

Two possible liquid-choking limits for artery-evaporator systems, the hydrodynamic limit $q_{\mathrm{CHF,h}}$ and the viscous-drag limit $q_{\mathrm{CHF,v}}$, are suggested and discussed. The $q_{\mathrm{CHF,h}}$ depends on the fluid properties and is inversely proportional to a flow-critical length scale corresponding to the coating macrostructure geometry. The

$q_{CHF,v}$ occurs when the viscous-drag on the liquid flow within the liquid supply artery (i.e., within the coating) exceeds the available capillary-gravity pumping. The q_{CHF} experienced by the coated surface is predicted to occur corresponding to the lower of the two liquid-choking limits for a given surface-coating-fluid system.

The hydrodynamic liquid-choking limit was given as

$$\frac{q_{CHF,h}}{\frac{\pi}{24}\rho_g^{1/2}\Delta h_{lg}[\sigma g(\rho_l-\rho_g)]^{1/4}} = \frac{3[\frac{\sigma}{g(\rho_l-\rho_g)}]^{1/4}}{\lambda_m^{1/2}}. \tag{2.55}$$

where λ_m is a length scale characterizing the vapor escape locations into the liquid pool from the porous-layer coating or surface. For a plain surface, λ_m depends on the balance between buoyancy and surface tension, and is then a function of fluid thermophysical properties. For surfaces with porous-layer coatings, λ_m is a function of geometrically determined vapor escape paths and is therefore a function of the porous structure.

The viscous-drag liquid-choking limit was given as

$$\frac{(q_{CHF,v})}{C_\theta \epsilon_s C_J \frac{\rho_l \sigma \Delta h_{lg}}{\mu_l}\frac{(K\epsilon)^{1/2}}{\delta_s}} = 1 - \frac{C_E}{C_J}\frac{\delta_s}{C_\theta^2 \epsilon_s^2 \epsilon^{1/2}}\frac{(q_{CHF,v})^2}{\rho_l \sigma \Delta h_{lg}^2}. \tag{2.49}$$

All of the liquid-choking limits presented in this work are graphically compared and shown with schematic depictions of the system and liquid and vapor flow paths in Fig. 4.4

The viscous-drag numerical model also provides a method for predicting the q versus $T_s - T_{lg}$ curve from a modulated porous-layer coating. Currently, the model underpredicts the q as a function of $T_s - T_{lg}$, but is considered in fair agreement with the experimental results. Some simplifying assumptions (e.g., those regarding the liquid-flow paths and the volume-averaging of the porous media) must be revised to bring the predictions into quantitative agreement.

For the surfaces tested in this study, the q_{CHF} is shown to be hydrodynamically limited. Predictions from Eq. (2.55), relating the critical heat flux with the appropriate modulation wavelength λ_m of the porous-layer coating, are in good agreement with the experimental results.

Further enhancement in the q_{CHF} of modulated porous-layer coatings is possible by reducing the modulation wavelength λ_m. Further experimental and theoretical investigations are required to determine the optimum modulation wavelength $\lambda_m = \lambda_{m,min}$.

Optimum enhancement in the $T_s - T_{lg}$ is possible by reducing the particle size, d, for a given modulation geometry.

Order of magnitude enhancement in theq_{CHF} from an artery-evaporation system would possibly be achieved by controlling the vapor escape paths to remove the limiting hydrodynamic mechanism.

5.3 Recommendations for Future Work

One result that is clear, and is in agreement with both the hydrodynamic and viscous-drag optimizations, is that the q_{CHF} will increase with decreasing d down to some minimum practical value. Determination of this minimum practical value is left for future efforts. Alternative or improved fabrication methods and alternative modulation patterns would enable the effect of particle size to be explored experimentally..

The minimum practical wavelength from Fig. 2.10 must also be determined. This is believed to be near in size to the particle diameter for a given system. Additional analyses involving the limits determined for use in heat pipe design might be considered as well, including the sonic limit for the vapor escape.

A number of assumptions were made in the development of the viscous-drag model and deserve reconsideration. One major assumption that warrants experimental verification is the separation of phases resulting in a completely saturated particle stack.

The ideas laid out in this work indicate that by completely separating the liquid and vapor flow paths, substantial enhancement in the q_{CHF} can be achieved. The design and fabrication of a capillary artery-evaporator system with completely separated flow paths should be investigated. Also, alternative applications of such systems (e.g., use in microgravity conditions) should also be explored. Not only would this would enable further verification that the viscous-drag model is independent of the hydrodynamic liquid-choking limit, but it would also greatly expand the applicability of the findings presented here.

BIBLIOGRAPHY

BIBLIOGRAPHY

[1] Incropera, F.P., "Liquid Emersion Cooling of Electronic Components," Heat Transfer in Electronic and Microelectronic Equipment, Ed. A.E. Bergles, Hemisphere Publishing Corporation, 407-444, 1990.

[2] Wataru, N., and A.E. Bergles, "Cooling Electronic Equipment: Past, Present, and Future," Heat Transfer in Electronic and Microelectronic Equipment, Ed. A.E. Bergles, Hemisphere Publ. Corp., 3-39, 1990.

[3] Bergles, A.E, "The Current Status of Heat Transfer Enhancement," Heat Transfer Enhancement and Energy Conversion, Ed. S.-J. Deng et al., Hemisphere Publ. Corp., 11-48, 1990.

[4] Thome, J. R., Enhanced Boiling Heat Transfer, Hemisphere Publishing Corporation, New York, 1990.

[5] Webb, R., Principles of Enhanced Heat Transfer, Wiley Interscience, New York, 1993.

[6] Bernardin, J. D., and I. Mudawar, "Film Boiling Heat Transfer of Droplet Streams and Sprays," Int. J. Heat Mass Transfer, Vol. 40, 2579-2593, 1997.

[7] Deb, S., and S.-C. Yao, "Analysis of Film Boiling Heat Transfer of Impacting Sprays," Int. J. Heat Mass Transfer, Vol. 32, 2099-2112, 1989.

[8] Wang, B. X., J. T. Zhang, and X. F. Peng, "Experimental Study on the Dryout Heat Flux of Falling Liquid Film," Int. J. Heat Mass Transfer, Vol. 43, No. 11, 1897-1903, 2000.

[9] Reay, D. A., Editor, Advances in Heat Pipe Techonology, Proceedings of the Ninth International Heat Pipe Conference, London 1981, Pergamon Press, 1982.

[10] Zhu, N., and K. Vafai, "Analysis of Cylindrical Heat Pipes Incorporating the Effects of Liquid-Vapor Coupling and Non-Darcian Transport – a Closed Form Solution," Int. J. Heat Mass Transfer, Vol. 42, 3405-3418, 1999.

[11] Zuo, Z. J., and A. Faghri, "A Network Thermodynamic Analysis of the Heat Pipe," Int. J. Heat Mass Transfer, Vol. 41, No. 11, 1473-1484, 1998.

[12] Miscevic, M., L. Tadrist, J. Pantaloni, and R. Yu, "Forced Convection Boiling Inside a Duct Filled with a Sintered Fibrous Medium," J. Porous Media, Vol. 1, No. 2, 135-146, 1998.

[13] Bergles, A. E., "What is the Real Mechanism of CHF in Pool Boiling?," Proc. Engineering Foundation Conf. on Pool and External Flow Boiling, Publ. by ASME, 165-170, 1992.

[14] Chang, J. Y. and S. M. You, "Boiling Heat Transfer Phenomena from Micro-Porous Surfaces in Saturated FC-72," Int. J. Heat Mass Transfer, Vol. 40, No. 18, 4437-4447, 1997.

[15] Lu, S. M., and R. H. Chang, "Pool Boiling from a Surface with a Porous Layer," AIChE J., Vol. 33, No. 11, 1813-1828, November 1987.

[16] Malyshenko, S. P., "Features of Heat Transfer with Boiling on Surfaces with Porous Coatings," Thermal Engineering, Vol. 38, No. 2, 81-88, 1991.

[17] O'Connor, J. P., and S. M. You, "A Painting Technique to Enhance Pool Boiling Heat Transfer in Saturated FC-72," ASME J. Heat Transfer, Vol. 117, 387-393, May 1995.

[18] Afgan, N. H., L. A. Jovic, S. A. Kovalev, and V. A. Lenykov, "Boiling Heat Transfer from Surfaces with Porous Layers," Int. J. Heat Mass Transfer, Vol. 28 No. 2, 415-422, 1985.

[19] Bergles, A. E. and M. C. Chyu, "Characteristics of Nucleate Pool Boiling from Porous Metallic Coatings," Trans. ASME J. Heat Transfer, Vol. 104, 279-285, May 1982.

[20] Kovalyov, S. A., and S. L. Soloviyov, "Heat Transfer and Critical Heat Fluxes in boiling on a Porous Surface," Heat Transfer - Soviet Research, Vol. 22, No. 3, 364-375, May-June 1990.

[21] Polezhaev, Y.V., and S.A. Kovalev, "Modeling Heat Transfer with Boiling on Porous Structures," Thermal Engineering, Vol. 37, No. 12, 617-620, 1990.

[22] Soloviyov, S.L., "Liquid Evaporation Heat Transfer on a Porous Surface," Heat Transfer - Soviet Research, Vol. 18, No. 3, 58-64, May-June 1986.

[23] Kaviany, M., Principles of Heat Transfer in Porous Media, Corrected Second Edition, Springer-Verlag, New York, 1999.

[24] Dunn, P. D., and D. A. Reay, Heat Pipes, Second Edition, Pergamon Press, 1978.

[25] Zuber, N., "Hydrodynamic Aspects of Boiling Heat Transfer," AECU-4439, Physics and Mathematics, U.S. Atomic Energy Commission, 1959.

[26] Udell, K. S., "Heat Transfer in Porous Media Considering Phase Change and Capillarity – the Heat Pipe Effect," Int. J. Heat Mass Transfer, Vol. 28, No. 2, 485-495, 1985.

[27] Chang, J. Y. and S. M. You, "Enhanced Boiling Heat Transfer from Micro-Porous Cylindrical Surfaces in Saturated FC-87 and R-123," Trans. ASME J. Heat Transfer, Vol. 119, 319-325, May 1997.

[28] Liter, S.G., and M. Kaviany, "CHF Enhancement by Modulated Porous-Layer Coating," Proc. of ASME 1998 IMECE, HTD vol. 361-1, pp 165-173, 1998.

[29] Gambill, W.R., and J.H. Lienhard, "An Upper-Bound for Critical Boiling Heat Fluxes," ASME J. Heat Transfer, Vol. 111, 815-818, 1989.

[30] Lienhard, J. H., and L. C. Witte, "An Historical Review of the Hydrodynamic Theory of Boiling," Rev. in Chem. Engin., Vol. 3, Nos. 3 & 4, 187-280, 1985.

[31] Lienhard, J. H., A Heat Transfer Textbook, 2nd Ed., Prentice-Hall, New Jersey, 1987.

[32] Kutateladze, S. S., Heat Transfer in Condensation and Boiling, Second Edition, AEC-tr-3770, 1952.

[33] Lienhard, J. H., and M. M. Hasan, "On Predicting Boiling Burnout with the Mechanical Energy Stability Criterion," ASME J. Heat Transfer, 276-279, May 1979.

[34] Haramura, Y., and Y. Katto, "A New Hydrodynamic Model of Critical Heat Flux Applicable Widely to Both Pool and Forced Convection Boiling on Submerged Bodies in Saturated Liquids," Int. J. Heat Mass Transfer, Vol. 26, No. 3, 389-399, 1983.

[35] Rohsenow, W., and P. Griffith, "Correlation of Maximum-heat-flux Data for Boiling for Saturated Liquids," Chem. Engin. Prog. Symp. Series, Vol. 52, No. 18, 1956.

[36] Carrica, P. M., and A. Clausse, "The Sudden Coalescence Model of the Boiling Crisis," ?, Saratoga, v4, 2425, 1995.

[37] Unal, C., P. Sadasivan, and R. A. Nelson, "On the Hot-Spot-Controlled Critical Heat Flux Mechanism in Pool Boiling of Saturated Fluids," Proc. Engineering Foundation Conf. on Pool and External Flow Boiling, Publ. by ASME, 151-164, 1992.

[38] Bar-Cohen, A., and A. McNeil, "Parametric Effects on Pool Boiling Critical Heat Flux in Dielectric Liquids," Proc. Engineering Foundation Conf. on Pool and External Flow Boiling, Publ. by ASME, 171-176, 1992.

[39] Dhir, V.K., "Boiling Heat Tranfser," Annu. Rev. Fluid Mech., Vol. 30, 365-401, 1998.

[40] Lienhard, J.H., and V.K. Dhir, "Hydrodynamic Prediction of Peak Pool-Boiling Heat Fluxes from Finite Bodies," ASME J. Heat Transfer, Series C, Vol. 95, 152-158, May 1973.

[41] Golobic, I., and A. E. Bergles, "Effects of Heater-Side Factors on the Saturated Pool Boiling Critical Heat Flux," Experimental Thermal and Fluid Science, Vol. 15, 43-51, 1997.

[42] Ha, S. J., and H. C. No, "A Dry-Spot Model of Critical Heat Flux in Pool and Vorced Convection Boiling," Int. J. Heat Mass Transfer, Vol. 41, No. 2, 303-311, 1998.

[43] Unal, C., P. Sadasivan, and R. A. Nelson, "On the Hot-Spot-Controlled Critical Heat Flux Mechanism in Saturated Pool Boiling: Part II - The influence of Contact Angle and Nucleation Site Density," Trans. of ASME J. Heat Transfer, Vol. 115, 813-816, August 1993.

[44] Carvalho, R. D. M., and A. E. Bergles, "The Effects of the Heater Thermal Conductance/Capacitance on the Pool Boiling o Saturated Fluids," Proc. Engineering Foundation Conf. on Pool and External Flow Boiling, Publ. by ASME, 151-164, 1992.

[45] Ferrel, J.K. and J. Alleavitch, "Vaporization Heat Transfer in Capillary Wick Structures," Chem. Engin. Prog. Symp. Series, Vol. 66, No. 102, 82-91, 1970.

[46] Whitaker, S., Fundamental Principles of Heat Transfer, Krieger Publishing Company, Malabar, 1983. Also, Kaviany, M., Principles of Heat Transfer, Course Pack, University of Michigan, 2000.

[47] Hsu, C.T., P. Chang, and K.W. Wong, "Modified Zehner-Schlunder Models for Stagnant Thermal Conductivity of Porous Media," Int. J. Heat Mass Transfer, Vol. 37, No. 17, pp 2751-2759, 1994.

[48] Beaton, C.F., and G.F. Hewitt, Editors, Physical Property Data for the Design Engineer, Hemisphere Publishing Corporation, New York, 1989.

[49] Kline, S. J., and F. A. McClintock, "Describing Uncertainties in Single-Sample Experiments," Mech. Engin., Vol. 75, 3-8, January 1953.